Computational analysis of MHD blood flow of SWCNT and MWCNT suspended nanofluid over a non-linear stretching sheet

Santosh Chaudhary[1], Ajay Singh[1] and Devendra Kumar[2,*]
[1]Department of Mathematics, Malaviya National Institute of Technology, Jaipur-302017, India
Email: d11.santosh@yahoo.com, ajaykaswaan21@gmail.com
[2]Department of Mathematics, University of Rajasthan, Jaipur-302004, India
Email: devendra.maths@gmail.com

December 29, 2023

Abstract

In this study, a computational analysis has been made for a steady, incompressible, MHD flow of the SWCNT-blood and the MWCNT-blood nanofluids past a non-linear stretching sheet of variable thickness. Darcy porous medium has been considered for fluid flow. Consequences of homogeneous-heterogeneous chemical reactions on heat and mass transfer along with Joule heating and viscous dissipation have been explored. Appropriate similarity transformations have been applied to convert the governing equations of nanofluid flow into non-linear ordinary differential equations. Galerkin finite element scheme has been used to examine the resulting system with corresponding boundary conditions. Numerical solutions of equations are demonstrated via graphs for various physical parameters, and these graphs have also been analyzed. Comparison of velocity, thermal, and concentration profiles of SWCNT-blood and MWCNT-blood nanofluids has been established. It is concluded that flow profiles of MWCNT-blood nanofluid dominate. Concentration profile declines with homogeneous and heterogeneous reaction parameters whereas increases with the Schimdt number for both nanofluids. Then, a comparison between present and the existing results was made, and they are in good agreement. After that, several physical quantities such as the local Nusselt number, skin friction coefficient, and concentration rate are exhibited in a table.

Keywords: MHD; Carbon nanotubes; Nanofluid; Stretching sheet

Nomenclatures

$A^\star$	Chemical species
$a^\star$	Concentration of chemical species $A^\star$
a_0	Positive constant
A	Ratio parameter
b	Dimensionless constant
B	Small constant
B_0	Magnitude of magnetic field strength
$B^\star$	Chemical species
$b^\star$	Concentration of chemical species $B^\star$
Br	Brinkman number
C_f	Skin friction coefficient
c_s	Heat capacity of the solid surface
C_p	Specific heat at constant pressure
D_A, D_B	Diffusion coefficients
Ec	Eckert number
F, f	Dimensionless stream function
k_1, k_s	Rate constants
$k^\star, k$	Permeability of porous medium
K	Homogeneous parameter
K_s	Heterogeneous parameter
m	Velocity power index parameter
M	Melting parameter
Nu_x	Local Nusselt number
Pr	Prandtl number
Re_m	Magnetic parameter
Re_x	Local Reynolds number
Sc	Schmidt number
T	Temperature of the fluid within the boundary layer
T_w	Melting surface temperature
T_∞	Ambient temperature
T_0	Temperature of the solid surface
u	Velocity component along $x-$axis
U_w	Non linear stretching velocity
U_e	Free stream velocity
U_∞, U_0	Reference velocities
v	Velocity component along $y-$axis
w_1, w_2, w_3	Weight functions
x	Direction parallel to the fluid flow
y	Direction perpendicular to the fluid flow

Greek symbols

α	Thermal diffusivity
$\alpha^\star$	Wall thickness parameter
δ	Ratio of diffusion coefficients

ρ	Density
σ_e	Electrical conductivity
κ	Thermal conductivity
λ	Latent heat of the nanofluid
ψ	Stream function
μ	Viscosity
ν	Kinematic viscosity
ϑ, Φ, φ	Dimensionless concentration
ϕ	Solid volume fraction
ψ_s	Shape function
Θ, θ	Dimensionless temperature
ξ	Similarity variable
Subscripts	
bf	Base fluid
nf	Nanofluid
CNT	Carbon nanotubes
Superscripts	
$\prime$	Derivative of the function

1 Introduction

The investigation of fluid behavior of the electrically conducting fluid in a magnetic field is known as magnetohydrodynamics (MHD). The investigation of MHD has been fascinating due to its extensive range of applications in various fields and the property of good heat transfer performance. The applications of MHD flow can be seen in petroleum production, turbines, liquid metal blankets, tritium breeding, and astrophysics sensors. Davidson (2001) appraised the MHD flow problems and explored the basics of MHD and its applications in engineering. After that, Bozkaya and Tezer-Sezgin (2007) brought an elemental solution for equations, which includes convection and diffusion. The impacts of thermal radiation on an unsteady flow are illustrated by Turkyilmazoglu (2011). Ellahi (2013) investigated the MHD non-Newtonian fluid flow. An MHD stagnation-point flow over a porous sheet has been examined by Jalilpour et al. (2014). Shehzad et al. (2015) perceived the impacts of convective heat on an MHD nanofluid flow. Numerical analysis of the MHD stagnation-point flow of a micropolar nanofluid using the Runge-Kutta fourth-order has been performed by Rashidi et al. (2016). Chaudhary et al. (2018) also discussed the MHD flow over a stretching sheet under the Newtonian and convective boundary restrictions. Chaudhary and Kanika (2020) scrutinized viscous dissipation and joule heating effects in a Marangoni boundary layer flow of an electrically conducting fluid in a magnetic field. Mehta et al. (2022) explored the MHD stagnation point stream flow past a vertical porous sheet along with heat generation, viscous dissipation, Joule heating, and thermal effect. Recently, Jain et al. (2023) investigated the MHD spinning fluid flow over a rotating disk with Brownian motion and inverse linear angular velocity.

Nowadays, the applications of nanoproducts are seen significantly in industries, while carbon nanotubes (CNTs) are among them. CNTs having high specific surface areas, high

mechanical strength, and a good conductor of electricity have appreciable applications in industries and other areas, for instance, medicine, sensors, delivery of DNA into cells, and composite materials. Initially, CNTs were explored by Lijima (1991). Wen and Ding (2004) tested the aqueous suspension of carbon nanotubes (CNTs) experimentally and found significant results in enhancing thermal conductivity. After that, Ding et al. (2006) examined the heat transfer capabilities of multi-walled CNT nanofluids. Many studies found that the surface friction is inferior for CNTs, which has been experimentally verified by Whiteby and Quirke (2007). Wang et al. (2008) studied the thermal effects on the vibration of CNTs delegating fluid using the Bernoulli-Euler beam model. The authenticity of different types of theoretical beam models is explored by Wang (2010). Khan et al. (2013) discussed the fluid flow and heat transfer in CNTs nanofluid by applying the Navier slip boundary condition. Further, the Marangoni convective MHD flow with viscous dissipation and joule heating is illustrated by Mahanthesh et al. (2017). Recently, Chaudhary and Kanika (2019) have numerically illustrated the SWCNT and MWCNT-based MHD flow.

To increase heat transfer capabilities, many efforts have been made by researchers. For the same, Choi and Eastman (1995) developed the notion of nanofluid. Nanofluid is a fluid composed of nanometer-sized solid nanoparticles and the base fluid. These nanoparticles are generally made of metals, oxides, and carbides such as Cu, Ag, and CuO. In various investigations, it has been spotted that the thermal conductivity of heat transfer fluid is enhanced when solid nanoparticles are added to traditional fluids. Due to the improved heat transfer capabilities, nanofluids have many applications in cancer therapy, microelectronics, and biomedicine. Initially, Zhou and Ni (2008) performed an experimental study to compute the specific heat capacity of nanofluid and indicated that nanoparticles and base fluid remain in equilibrium in the nanofluid system. The steady boundary layer of a nanofluid over a moving flat plate has been investigated analytically by Bachok et al. (2010). Ahmed et al. (2011) paid their attention to the enlargement in heat transfer in a corrugated channel due to nanofluids. They illustrated it for distinct values of the Reynolds number. The unsteady mixed convection flow and heat transfer of nanofluids past a stretching surface have been numerically analyzed by Mahdy (2012). Rashidi et al. (2014) demonstrated the Buoyancy impact on the MHD flow of an incompressible viscous nanofluid, and non-linear governing equations are numerically handled by the shooting technique. The impact of thermal radiation on an MHD nanofluid flow was explored by Sheikholeslami et al. (2015). They also investigated the heat transfer between two parallel plates. Further, Turkyilmazoglu (2016) explored the efficiency of direct absorption solar collectors using nanofluid, and Ghalandari et al. (2019) illustrated the numerical simulation of nanofluid flow. Chaudhary (2022) examined the impact of nanoparticle shape over a moving plate. The effect of thermal radiation, convective boundary condition, and Brownian motion on the electro-magnetohydrodynamic(EMHD) flow of nanofluid with the Darcy-Forchheimer porous medium has been reported by Chaudhary and Chouhan (2023). Jangid et al. (2023) discussed the MHD flow of Williamson nanofluid past a permeable stretching sheet with buoyancy force, thermal radiation, and Joule heating.

The exploration of heat transformation through the boundary layer over a stretching sheet has attracted scientists to study the important concept due to its many practical uses in diverse fields of science and engineering. Some stretching surface applications include

thermal insulation, solar collectors, glass-fiber and paper production, food processing, and plasma studies. Initially, flow along a stretching sheet was reported by Crane (1970). Further, Mahapatra and Gupta (2002) investigated heat transfer in stagnation-point flow due to a stretching sheet stretched in its plane. The hydromagnetic flow of a micropolar fluid past a stretching surface is explored by Kumar (2009), and for solving the system of governing equations, he used the finite element method. Bachok et al. (2010) reported the steady stagnation-point flow numerically along with a linear stretching/shrinking sheet. A dusty fluid flow over a stretching sheet is illustrated by Gireesha et al. (2011) while considering the influence of heat source/sink. Noghrehabadi et al. (2013) discussed the impacts of thermal convective boundary restrictions on boundary layer flow and heat transfer of nanofluids via a stretching sheet. Further, Noor et al. (2015) and Hsiao (2016) paid their attention to the mixed convection stagnation point flow having slip boundaries by taking different stretching sheets. After that, Chaudhary and Choudhary (2018) illustrated a flow problem along with a stretching sheet with thermal radiation. Recently, Kumar et al. (2023) reported the MHD flow of micropolar liquid over a porous stretching sheet along with heat source, thermal radiation, and slip boundary conditions.

The review of the above-mentioned literature concludes that the study of the influence of homogeneous-heterogeneous chemical reaction on heat and mass transfer of an electro-hydrodynamic flow of nanofluid over a non-linear stretching sheet has not been explored yet. The thickness of the sheet is taken to be variable. The effect of Joule heating and viscous dissipation on heat transfer has been considered. The suspension of SWCNT and MWCNT in human blood has been taken into account. The CNTs have been chosen as nanoparticles due to their high thermal conductivity, exceptional corrosion resistance, and mechanical strength. The Galerkin finite element method is employed to numerically solve the system of equations. The consequences of various controlling parameters are shown visually for velocity, thermal, and concentration profiles. The numeric values of the local skin friction coefficient, Nusselt number, and Sherwood number are presented in the table. The accuracy of the results obtained in the present study is verified with already published work.

2 Problem description

Let us take a steady, two-dimensional, electro-hydrodynamic boundary layer flow of viscous, incompressible nanofluid over a porous non-linear stretching sheet with a variable thickness $y = B(x+b)^{\frac{1-m}{2}}$. B is a small constant, b is a non-dimensional constant, and m is a velocity power index. In addition, the flow is affected by viscous dissipation and ohmic heating. A combination of homogeneously distributed nanoparticles SWCNT and MWCNT in the base fluid− human blood is used as a nanofluid. As demonstrated in Fig. 1, a cartesian coordinate system (x, y) is considered in which carbon nanotubes− SWCNT and MWCNT are also shown symbolically. The $x-$axis is taken in the direction of motion of the non-linear stretching surface, and the $y-$axis is vertical. The flow is bounded in the upper half-plane $y > 0$. A magnetic field of constant strength B_0 is supposed to be used orthogonal to the surface. The induced magnetic field is negligible if the magnetic Reynolds number is minimal. The non-linear stretching velocity $U_w = U_0(x+b)^m$ and free

stream velocity $U_e = U_\infty(x+b)^m$ are considered, here U_0 and U_∞ are the reference velocities. Melting surface temperature T_w is taken to be less than the ambient temperature T_∞. The heat produced throughout the irreversible chemical reaction is not taken into account.

The homogeneous cubic autocatalytic reaction is

$$A^\star + 2B^\star \to 3B^\star, \quad rate = k_1 a^\star b^{\star 2} \tag{1}$$

while on the catalyst surface, the heterogeneous reaction of the first order is as

$$A^\star \to B^\star, \quad rate = k_s a^\star \tag{2}$$

here $a^\star$ and $b^\star$ indicate the concentrations of chemical species $A^\star$ and $B^\star$, respectively, while k_1 and k_s are the rate constants. The reaction rate tends to be zero at the external and outer edges of the boundary layer flow. Under these assumptions, the governing equations for the problem are described as

$$\frac{\partial u}{\partial x} + \frac{\partial v}{\partial y} = 0 \tag{3}$$

$$u\frac{\partial u}{\partial x} + v\frac{\partial u}{\partial y} = U_e\frac{dU_e}{dx} + \nu_{nf}\left[\frac{\partial^2 u}{\partial y^2} - \frac{u}{k} - \frac{(\sigma_e)_{nf}B_0^2}{\mu_{nf}}(u - U_e)\right] \tag{4}$$

$$u\frac{\partial T}{\partial x} + v\frac{\partial T}{\partial y} = \frac{1}{(\rho C_p)_{nf}}\left[\kappa_{nf}\frac{\partial^2 T}{\partial y^2} + \mu_{nf}\left(\frac{\partial u}{\partial y}\right)^2 + (\sigma_e)_{nf}B_0^2(u - U_e)^2\right] \tag{5}$$

$$u\frac{\partial a^\star}{\partial x} + v\frac{\partial a^\star}{\partial y} = D_A\frac{\partial^2 a^\star}{\partial y^2} - k_1 a^\star b^{\star 2} \tag{6}$$

$$u\frac{\partial b^\star}{\partial x} + v\frac{\partial b^\star}{\partial y} = D_B\frac{\partial^2 b^\star}{\partial y^2} + k_1 a^\star b^{\star 2} \tag{7}$$

with the boundary conditions

$$\begin{aligned} y = B(x+b)^{(1-m)/2}: \quad & u = U_w(x), \quad v = 0, \quad T = T_w, \\ & \kappa_{nf}\frac{\partial T}{\partial y} = \rho_{nf}\left[\lambda + c_s(T_w - T_0)\right]v, \\ & D_A\frac{\partial a^\star}{\partial y} = k_s a^\star, \quad D_B\frac{\partial b^\star}{\partial y} = -k_s a^\star \\ y \to \infty: \quad & u \to U_e(x), \quad T \to T_\infty, \quad a^\star \to a_0, \quad b^\star \to 0 \end{aligned} \tag{8}$$

In the above equation, subscript nf indicates the thermophysical characteristics of nanofluid, u, and v denote the velocity components along the $x-$ and $y-$ directions, respectively, $\nu(=\frac{\mu}{\rho})$ is the kinematic viscosity, μ is the dynamic viscosity, ρ is the density, k is the permeability of the porous medium, σ_e stands for the electrical conductivity, T indicate the temperature of nanofluid, C_p stands for the specific heat at constant pressure, κ is indicating the thermal conductivity, D_A, and D_B indicate diffusion coefficients, λ represent the latent heat of the nanofluid, c_s, and T_0 are the heat capacity of the solid surface and temperature, respectively, and a_0 is a positive constant.

Based on the theoretical model, physical properties of the $CNTs-$human blood nanofluid (represented in Table I) are mentioned by Khalid et al. (2018) as

$$\frac{\mu_{nf}}{\mu_{bf}} = \frac{1}{(1-\phi)^{5/2}} \tag{9}$$

$$\frac{\rho_{nf}}{\rho_{bf}} = 1-\phi+\frac{\rho_{CNT}}{\rho_{bf}}\phi \tag{10}$$

$$\frac{(\sigma_e)_{nf}}{(\sigma_e)_{bf}} = 1+\frac{3\left[\frac{(\sigma_e)_{CNT}}{(\sigma_e)_{bf}}-1\right]\phi}{2+\frac{(\sigma_e)_{CNT}}{(\sigma_e)_{bf}}-\left[\frac{(\sigma_e)_{CNT}}{(\sigma_e)_{bf}}-1\right]\phi} \tag{11}$$

$$\frac{(\rho C_p)_{nf}}{(\rho C_p)_{bf}} = 1-\phi+\frac{(\rho C_p)_{CNT}}{(\rho C_p)_{bf}}\phi \tag{12}$$

$$\frac{\kappa_{nf}}{\kappa_{bf}} = \frac{1-\phi+2\frac{\kappa_{CNT}}{\kappa_{CNT}-\kappa_{bf}}ln\frac{\kappa_{CNT}+\kappa_{bf}}{2\kappa_{bf}}\phi}{1-\phi+2\frac{\kappa_{bf}}{\kappa_{CNT}-\kappa_{bf}}ln\frac{\kappa_{CNT}+\kappa_{bf}}{2\kappa_{bf}}\phi} \tag{13}$$

where subscripts bf and CNT are used for base fluid human blood and carbon nanotubes, respectively, and ϕ indicates the volume fraction of $CNTs$.

3 Transformations

Utilizing the non-dimensional variables given by Hayat et al. (2016) are as follows.

$$\begin{aligned}&\psi = \left[\frac{2}{m+1}\nu_{bf}U_0(x+b)^{m+1}\right]^{\frac{1}{2}}F(\xi), \quad \xi = \left[\frac{m+1}{2}\frac{U_0(x+b)^{m-1}}{\nu_{bf}}\right]^{\frac{1}{2}}y,\\ &T = T_w+(T_\infty-T_w)\Theta(\xi), \quad a^\star = a_0\,\vartheta(\xi), \quad b^\star = a_0\,\Phi(\xi)\end{aligned} \tag{14}$$

here $\psi(x,y)$ denotes the stream function, which identically satisfies the mass conservation Eq. (3) along with $u=\frac{\partial\psi}{\partial y}$ and $v=-\frac{\partial\psi}{\partial x}$, $F(\xi)$ is the dimensionless stream function, ξ is the similarity variable, $\Theta(\xi)$ is the dimensionless temperature and, $\vartheta(\xi)$ and $\varphi(\xi)$ are the dimensionless concentrations. Because of the above similarity variables Eq. (14), the Eqs. (4) to (8) are reduced to

$$\begin{aligned}&\frac{1}{(1-\phi)^{5/2}}F'''+\left(1-\phi+\frac{\rho_{CNT}}{\rho_{bf}}\phi\right)\left(FF''-\frac{2m}{1+m}F'^2+\frac{2m}{1+m}A^2\right)\\ &\qquad-\frac{2k^\star}{1+m}\frac{1}{(1-\phi)^{5/2}}F'-\frac{(\sigma_e)_{nf}}{(\sigma_e)_{bf}}\frac{2}{1+m}Re_m\,(F'-A)=0\end{aligned} \tag{15}$$

$$\begin{aligned}&\frac{\kappa_{nf}}{\kappa_{bf}}\Theta''+Pr\left[1-\phi+\frac{(\rho C_p)_{CNT}}{(\rho C_p)_{bf}}\phi\right]F\Theta'+\frac{1}{(1-\phi)^{5/2}}BrF''^2\\ &\qquad+\frac{(\sigma_e)_{nf}}{(\sigma_e)_{bf}}\frac{2}{1+m}BrRe_m(F'-A)^2=0\end{aligned} \tag{16}$$

$$\frac{1}{Sc}\vartheta''+F\vartheta'-\frac{2K}{1+m}\Phi^2\vartheta=0 \tag{17}$$

$$\frac{\delta}{Sc}\Phi'' + F\Phi' + \frac{2K}{1+m}\vartheta\Phi^2 = 0 \tag{18}$$

with the transformed boundary conditions

$$\begin{aligned}
\alpha^\star = B\left(\frac{1+m}{2}\frac{U_0}{\nu_{bf}}\right)^{\frac{1}{2}}: \quad & F = \frac{1-m}{1+m}\alpha^\star, \quad F' = 1, \quad \Theta = 0, \\
& \frac{\kappa_{nf}}{\kappa_{bf}}M\Theta' + Pr\left(1-\phi+\frac{\rho_{CNT}}{\rho_{bf}}\phi\right)\left(F - \frac{1-m}{1+m}\alpha^\star\right) = 0, \\
& \vartheta' = \left(\frac{2}{1+m}\right)^{\frac{1}{2}} K_s\vartheta, \quad \Phi' = -\left(\frac{2}{1+m}\right)^{\frac{1}{2}}\frac{K_s}{\delta}\vartheta \\
\alpha^\star \to \infty: \quad & F' \to A, \quad \Theta \to 1, \quad \vartheta \to 1, \quad \Phi \to 0
\end{aligned} \tag{19}$$

In the above expressions, prime ($'$) represents the derivatives of functions with respect to ξ, $A\ (= \frac{U_\infty}{U_0})$ is the ratio parameter, $k^\star\ \left[= \frac{\nu_{bf}}{kU_0(x+b)^{m-1}}\right]$ is representing the permeability of the porous media, $Re_m\ \left[= \frac{(\sigma_e)_{bf}{B_0}^2(x+b)}{\rho_{bf}U_w}\right]$ is the magnetic parameter, $Pr\ \left[= \left(\frac{\nu\rho C_p}{\kappa}\right)_{bf}\right]$ is the Prandtl number, $Br\ (= PrEc)$ is the Brinkman number, $Ec\ \left[= \frac{U_w^2}{(C_p)_{bf}(T_\infty - T_w)}\right]$ stands for the Eckert number, $Sc\ \left(= \frac{\nu_{bf}}{D_A}\right)$ indicates the Schmidt number, $K\ \left[= \frac{k_1{a_0}^2(x+b)}{U_w}\right]$ is the homogeneous parameter, $\delta\ \left(= \frac{D_B}{D_A}\right)$ is the ratio of diffusion coefficients, $\alpha^\star\ (= \xi)$ is the wall thickness parameter, $M\ \left[= \frac{(C_p)_{bf}(T_\infty - T_w)}{[\lambda + c_s(T_w - T_0)]}\right]$ is the melting parameter, and $K_s\ \left\{= \frac{k_s}{D_A}\left[\frac{\nu_{bf}(x+b)}{U_w}\right]^{\frac{1}{2}}\right\}$ is the heterogeneous parameter. Additionally, in many applications, the diffusion coefficients D_A and D_B are equal, i.e., $\delta = 1$. Eqs. (17) and (18) are reduced to

$$\vartheta'' + Sc\,F\vartheta' - \frac{2}{1+m}K\,Sc\,\vartheta(1-\vartheta)^2 = 0 \tag{20}$$

with $\vartheta + \Phi = 1$

Applying $F(\xi) = f(\xi - \alpha^\star) = f(\eta), \quad \Theta(\xi) = \theta(\xi - \alpha^\star) = \theta(\eta)$
and $\Phi(\xi) = \varphi(\xi - \alpha^\star) = \varphi(\eta)$

Eqs. (15), (16) and (20) with boundary condition Eq. (19) give

$$\begin{aligned}
\frac{1}{(1-\phi)^{5/2}}f''' + \left(1-\phi+\frac{\rho_{CNT}}{\rho_{bf}}\phi\right)\left(ff'' - \frac{2m}{1+m}f'^2 + \frac{2m}{1+m}A^2\right) \\
- \frac{2k^\star}{1+m}\frac{1}{(1-\phi)^{5/2}}f' - \frac{(\sigma_e)_{nf}}{(\sigma_e)_{bf}}\frac{2}{1+m}Re_m\,(f'-A) = 0
\end{aligned} \tag{21}$$

$$\begin{aligned}
\frac{\kappa_{nf}}{\kappa_{bf}}\theta'' + Pr\left[1-\phi+\frac{(\rho C_p)_{CNT}}{(\rho C_p)_{bf}}\phi\right]f\theta' + \frac{1}{(1-\phi)^{5/2}}Brf''^2 \\
+ \frac{(\sigma_e)_{nf}}{(\sigma_e)_{bf}}\frac{2}{1+m}BrRe_m(f'-A)^2 = 0
\end{aligned} \tag{22}$$

$$\varphi'' + Sc\,f\varphi' - \frac{2}{1+m}K\,Sc\,\varphi(1-\varphi)^2 = 0 \tag{23}$$

along with the associated boundary conditions

$$\begin{aligned}
\eta = 0: \quad & f = \frac{1-m}{1+m}\alpha^{\star}, \quad f' = 1, \quad \theta = 0, \\
& \frac{\kappa_{nf}}{\kappa_{bf}} M\theta' + Pr\left(1 - \phi + \frac{\rho_{CNT}}{\rho_f}\phi\right)\left(f - \frac{1-m}{1+m}\alpha^{\star}\right) = 0, \\
& \varphi' = \left(\frac{2}{m+1}\right)^{1/2} K_s \varphi \\
\eta \to \infty: \quad & f' \to A \quad , \quad \theta \to 1 \quad , \quad \varphi \to 1
\end{aligned} \tag{24}$$

here, prime represents the differentiation with respect to η.

4 Physical Quantities

Here, we discuss the physical quantities such as the local skin friction coefficient (C_f) and local Nusselt number (Nu_x), which indicate the flow and heat transfer, respectively and symbolic as (mathematical notation)

$$C_f = \frac{2\mu_{nf}}{\rho_{bf}{U_w}^2}\left(\frac{\partial u}{\partial y}\right)_{y=B(x+b)^{(1-m)/2}}, \quad Nu_x = -\frac{\kappa_{nf}(x+b)}{\kappa_{bf}(T_\infty - T_w)}\left(\frac{\partial T}{\partial y}\right)_{y=B(x+b)^{(1-m)/2}} \tag{25}$$

By employing the similarity transformations Eq. (14), the Eq. (25) can be expressed as

$$\frac{C_f}{Re_x^{-1/2}} = \frac{2}{(1-\phi)^{5/2}}\left(\frac{1+m}{2}\right)^{1/2} f''(0), \quad \frac{Nu_x}{Re_x^{1/2}} = -\frac{\kappa_{nf}}{\kappa_{bf}}\left(\frac{1+m}{2}\right)^{1/2}\theta'(0) \tag{26}$$

where, $Re_x \left[= \frac{U_w(x+b)}{\nu_{bf}}\right]$ is the local Reynolds number.

5 Computational method and accuracy

Eqs. (21) to (23) with the boundary conditions Eq. (24) are handled numerically by employing the Galerkin finite element scheme as depicted by the flow diagram in Fig. 2, which is a well-known computational approach for handling differential equations. The basic idea behind this technique is that the whole domain is discretized into linear elements, and after that, equations are obtained for each element. Furthermore, element equations are assembled, and the equations have been reduced by applying boundary conditions. The remaining equations are handled by using the appropriate technique.

Assume

$$f' = p \tag{27}$$

then Eqs. (21) to (23) are reduced into the below form

$$\frac{1}{(1-\phi)^{5/2}}p'' + \left(1-\phi+\frac{\rho_{CNT}}{\rho_{bf}}\phi\right)\left(fp' - \frac{2m}{1+m}p^2 + \frac{2m}{1+m}A^2\right) - \frac{2k^\star}{1+m}\frac{1}{(1-\phi)^{5/2}}p - \frac{(\sigma_e)_{nf}}{(\sigma_e)_{bf}}\frac{2}{1+m}Re_m\,(p-A) = 0 \tag{28}$$

$$\frac{\kappa_{nf}}{\kappa_{bf}}\theta'' + Pr\left[1-\phi+\frac{(\rho C_p)_{CNT}}{(\rho C_p)_{bf}}\phi\right]f\theta' + \frac{1}{(1-\phi)^{5/2}}Br\,p'^2 + \frac{(\sigma_e)_{nf}}{(\sigma_e)_{bf}}\frac{2}{1+m}BrRe_m(p-A)^2 = 0 \tag{29}$$

$$\varphi'' + Sc\,f\varphi' - \frac{2K}{1+m}Sc\,\varphi(1-\varphi)^2 = 0 \tag{30}$$

and the changed boundary conditions are

$$\begin{aligned}\eta = 0: \quad & f = \left(\frac{1-m}{1+m}\right)\alpha^\star,\ p = 1,\ \theta = 0,\ \varphi' = \left(\frac{2}{1+m}\right)^{1/2}K_s\varphi,\\ & \frac{\kappa_{nf}}{\kappa_{bf}}M\theta' + \left(1-\phi+\frac{\rho_{CNT}}{\rho_{bf}}\phi\right)Pr\left[f - \frac{1-m}{1+m}\alpha^\star\right] = 0\\ \eta\to\infty: \quad & p\to A, \quad \theta\to 1, \quad \varphi\to 1\end{aligned} \tag{31}$$

If the values of η are taken larger than 6, then there are no further changes in the solutions of the system. Keeping this fact and limitations of computation, without loss of generality, $\eta\to\infty$ is taken numerically as $\eta_{max} = 6$. The flow domain is divided into 1,000 linear elements of equal sizes. A typical element (η_r, η_{r+1}) (say) is considered over this element, Eqs. (27) to (30) can be written in the variational form and are defined as follows

$$\int_{\eta_r}^{\eta_{r+1}} w_1(f'-p) = 0 \tag{32}$$

$$\int_{\eta_r}^{\eta_{r+1}} w_2\left[\frac{1}{(1-\phi)^{5/2}}p'' + \left(1-\phi+\frac{\rho_{CNT}}{\rho_{bf}}\phi\right)\left(fp' - \frac{2m}{1+m}p^2 + \frac{2m}{1+m}A^2\right) - \frac{2k^\star}{1+m}\frac{1}{(1-\phi)^{5/2}}p - \frac{(\sigma_e)_{nf}}{(\sigma_e)_{bf}}\frac{2}{1+m}Re_m\,(p-A)\right]d\eta = 0 \tag{33}$$

$$\int_{\eta_r}^{\eta_{r+1}} w_3\left\{\frac{\kappa_{nf}}{\kappa_{bf}}\theta'' + Pr\left[1-\phi+\frac{(\rho C_p)_{CNT}}{(\rho C_p)_{bf}}\phi\right]f\theta' + \frac{1}{(1-\phi)^{5/2}}Br\,p'^2 + \frac{(\sigma_e)_{nf}}{(\sigma_e)_{bf}}\frac{2}{1+m}BrRe_m(p-A)^2\right\}d\eta = 0 \tag{34}$$

$$\int_{\eta_r}^{\eta_{r+1}} w_4\left[\varphi'' + Sc\,f\varphi' - \frac{2K}{1+m}Sc\,\varphi(1-\varphi)^2\right]d\eta = 0 \tag{35}$$

here w_1, w_2, w_3, and w_4 are weight functions corresponding to the functions f, p, θ, and φ, respectively and these functions are given by:

$$\begin{aligned} f &= \sum_{t=1}^{2} f_t \psi_t, \qquad p = \sum_{t=1}^{2} p_t \psi_t, \qquad \theta = \sum_{t=1}^{2} \theta_t \psi_t, \\ \varphi &= \sum_{t=1}^{2} \varphi_t \psi_t \end{aligned} \tag{36}$$

While $w_1 = w_2 = w_3 = w_4 = \psi_s$, s = 1,2,3,4

The shape function ψ_s, for a typical element (η_r , η_{r+1}), is defined as:

$$\psi_1{}^{(r)} = \frac{\eta_{r+1} - \eta}{\eta_{r+1} - \eta_r}, \quad \psi_2{}^{(r)} = \frac{\eta - \eta_r}{\eta_{r+1} - \eta_r}, \quad \eta_r \le \eta \le \eta_{r+1} \tag{37}$$

In matrix form the system of Eqs. (32)-(35) are represented by

$$\begin{bmatrix} [A_{11}] & [A_{12}] & [A_{13}] & [A_{14}] \\ [A_{21}] & [A_{22}] & [A_{23}] & [A_{24}] \\ [A_{31}] & [A_{32}] & [A_{33}] & [A_{34}] \\ [A_{41}] & [A_{42}] & [A_{43}] & [A_{44}] \end{bmatrix} \begin{bmatrix} \{f\} \\ \{p\} \\ \{\theta\} \\ \{\varphi\} \end{bmatrix} = \begin{bmatrix} \{b^1\} \\ \{b^2\} \\ \{b^3\} \\ \{b^4\} \end{bmatrix} \tag{38}$$

where $[A^{ij}]$ and $\{b^i\}$, $i = 1, 2, 3, 4$, are as follows:

$$A_{st}^{11} = \int_{\eta_r}^{\eta_{r+1}} \psi_s \frac{d\psi_t}{d\eta} d\eta,$$

$$A_{st}^{12} = -\int_{\eta_r}^{\eta_{r+1}} \psi_s \psi_t d\eta,$$

$$A_{st}^{13} = A_{st}^{14} = A_{st}^{21} = 0,$$

$$\begin{aligned} A_{st}^{22} = \int_{\eta_r}^{\eta_{r+1}} \Bigg[& -\frac{1}{(1-\phi)^{5/2}} \frac{d\psi_s}{d\eta} \frac{d\psi_t}{d\eta} \\ & + \left(1 - \phi + \frac{\rho_{CNT}}{\rho_{bf}} \phi\right) \left(\bar{f} \psi_s \frac{d\psi_t}{d\eta} - \frac{2m}{1+m} \bar{p} \psi_s \psi_t\right) \\ & - \frac{2k^\star}{1+m} \frac{1}{(1-\phi)^{5/2}} \psi_s \psi_t - \frac{(\sigma_e)_{nf}}{(\sigma_e)_{bf}} \frac{2}{1+m} Re_m \psi_s \psi_t \Bigg] d\eta, \end{aligned}$$

$$A_{st}^{23} = A_{st}^{24} = A_{st}^{31} = 0,$$

$$\begin{aligned} A_{st}^{32} = \int_{\eta_r}^{\eta_{r+1}} \Bigg\{ & \frac{1}{(1-\phi)^{5/2}} Br\, \bar{p}'\, \psi_s \frac{d\psi_t}{d\eta} \\ & + \frac{(\sigma_e)_{nf}}{(\sigma_e)_{bf}} \frac{2}{1+m} Br Re_m \left(\bar{p} - 2A\right) \psi_s \psi_t \Bigg\} d\eta, \end{aligned}$$

$$A_{st}^{33}=\int_{\eta_r}^{\eta_{r+1}}\left\{-\frac{\kappa_{nf}}{\kappa_{bf}}\frac{d\psi_s}{d\eta}\frac{d\psi_t}{d\eta}+Pr\left[1-\phi+\frac{(\rho C_p)_{CNT}}{(\rho C_p)_{bf}}\phi\right]\bar{f}\psi_s\frac{d\psi_t}{d\eta}\right\}d\eta,$$

$$A_{st}^{34}=A_{st}^{41}=A_{st}^{42},A_{st}^{43}=0,$$

$$A_{st}^{44}=\int_{\eta_r}^{\eta_{r+1}}\left\{-\frac{d\psi_s}{d\eta}\frac{d\psi_t}{d\eta}+Sc\bar{f}\psi_s\frac{d\psi_t}{d\eta}-\frac{2K}{1+m}Sc\left[\left(\bar{\varphi}-2\right)\bar{\varphi}\psi_s\psi_t+\psi_s\psi_t\right]\right\}d\eta$$

and

$$b_s^1=0,$$

$$b_s^2=-\frac{1}{(1-\phi)^{5/2}}\left(\psi_s\frac{dp}{d\eta}\right)_{\eta_r}^{\eta_{r+1}}-\frac{(\sigma_e)_{nf}}{(\sigma_e)_{bf}}\frac{2}{1+m}Re_mA\int_{\eta_r}^{\eta_{r+1}}\psi_sd\eta$$
$$-\frac{2m}{1+m}A^2\left(1-\phi+\frac{\rho_{CNT}}{\rho_f}\phi\right)\int_{\eta_r}^{\eta_{r+1}}\psi_sd\eta,$$

$$b_s^3=-\frac{\kappa_{nf}}{\kappa_{bf}}\left(\psi_s\frac{d\theta}{d\eta}\right)_{\eta_r}^{\eta_{r+1}}-\frac{(\sigma_e)_{nf}}{(\sigma_e)_{bf}}\frac{2}{1+m}BrRe_mA^2\int_{\eta_r}^{\eta_{r+1}}\psi_sd\eta,$$

$$b_s^4=-\left(\psi_s\frac{d\varphi}{d\eta}\right)_{\eta_r}^{\eta_{r+1}},$$

Where

$$\bar{f}=\sum_{s=1}^{s=2}\bar{f}_s\psi_s\quad,\quad\bar{p}=\sum_{s=1}^{s=2}\bar{p}_s\psi_s,$$
$$\bar{p'}=\sum_{s=1}^{s=2}\bar{p'_s}\psi_s\quad,\quad\bar{\varphi}=\sum_{s=1}^{s=2}\bar{\varphi}_s\psi_s$$

As mentioned, the whole domain is divided into 1,000 linear elements of equal sizes. There are 1001 nodes, and four functions are to be evaluated at each node. Hence, after assembling all the element equations, a matrix is obtained with the order of 4004×4004. After implementing boundary conditions, the system has 3,996 equations that are solved by the Gauss elimination technique while the accuracy of 10^{-7} is maintained.

To ensure precision, credibility, and consistency, we have compared our numerical outcomes with the reported data of Hayat et al. (2016) by imposing some conditions. The comparative results have been shown in Table II, and the accuracy of that validated our numerical computations.

6 Analysis of the Results

This part demonstrates the graphical rendition for viewing the effects of sundry parameters on the velocity, temperature, and concentration distributions of the SWCNT (single-wall carbon nanotube) and MWCNT (multi-wall carbon nanotube) suspended nanofluids by taking base fluid as blood. Also, the values of wall shear stress $f''(0)$, wall heat flux $\theta'(0)$

and concentration rate $\varphi'(0)$, corresponding to changes in physical parameters like power index parameter (m), wall thickness parameter $(\alpha^\star)$, ratio parameter (A), volume fraction parameter (ϕ), permeability parameter $(k^\star)$, magnetic parameter (Re_m), the Brinkman number (Br), the heterogeneous parameter (K_s), the Schmidt number (Sc), and the homogeneous parameter (K), keeping the Prandtl number $Pr(= 25)$ as constant are shown in Table III. Other parameters are taken as constant for unveiling the effect of specific parameters. It is noticed that for the considered profiles as the velocity, temperature, and concentration, MWCNT nanofluid is dominated when compared with SWCNT nanofluid.

Figs. 3−5 are sketched to see the behavior of flow velocity $f'(\eta)$, temperature $\theta(\eta)$, and concentration $\varphi(\eta)$ distributions for various values of power index parameter m, respectively. We notice that velocity $f'(\eta)$ decreases along with the increment in power index parameter m when $\eta < 1.5$ for both SWCNT and MWCNT, while the opposite behavior can be seen when $\eta \geq 1.5$. Increasing the power index parameter m reduces temperature distribution for SWCNT and MWCNT. The concentration profile is shown to have increments along with incremental changes in power index parameter m for both SWCNT and MWCNT. Physically, the enhancement in the power index parameter leads to an increase in the wall thickness parameter. Due to this, a reduction in the stretching of the surface occurs; hence the flow velocity $f'(\eta)$ decreases when $\eta < 1.5$, while if $\eta \geq 1.5$, there is an increment in the stretching of the surface, so the flow velocity $f'(\eta)$ increases. Furthermore, the reduction in the stretching surface leads to a reduction in the thermal boundary layer. Therefore the decrement happens in temperature. Similarly, the stretching of the surface is also a reason behind the increment in concentration profile.

The effect of wall thickness parameter $\alpha^\star$ on the velocity $f'(\eta)$, temperature $\theta(\eta)$, and concentration $\varphi(\eta)$ profiles are displayed in Figs. 6−8, respectively. The velocity of the fluid $f'(\eta)$ enlarges along with the rising values of the wall thickness parameter $\alpha^\star$, while a reduction in both temperature $\theta(\eta)$ and concentration $\varphi(\eta)$ is observed for both types of nanofluids. As the wall thickness parameter enhances, the dynamic viscosity increases and as a consequence, velocity $f'(\eta)$ grows significantly. In contrast, a reduction can be seen in temperature $\theta(\eta)$ and concentration $\varphi(\eta)$.

Figs. 9−11 portray the impact of ratio parameter A on the flow field $f'(\eta)$, temperature field $\theta(\eta)$, and concentration field $\varphi(\eta)$, respectively. It is noted that the flow field $f'(\eta)$, temperature field $\theta(\eta)$, and concentration field $\varphi(\eta)$ enhance along with the increasing values of ratio parameter A for both types of nanofluids. Due to the enlargement in the ratio parameter, the free stream velocity increases to the stretching velocity. Hence, the flow changed in inverted boundary layer fabrication, resulting in the rise in velocity profile $f'(\eta)$. At the same time, dynamic pressure increment leads to a fall off in the temperature profile $\theta(\eta)$.

The impacts of various values of volume fraction parameter ϕ on the dimensionless velocity $f'(\eta)$, temperature $\theta(\eta)$, and concentration $\varphi(\eta)$ are plotted in Figs. 12−14, respectively. These figures have shown that velocity $f'(\eta)$ and concentration $\varphi(\eta)$ have the behavior of acceleration with the enhancing values of volume fraction parameter ϕ. In contrast, the dimensionless temperature decelerates for SWCNT and MWCNT. The nanoparticle volume fraction is directly related to convective flow, so velocity increment happens. Due to the convection effect, the heat transfers from the hot fluid flow to a relatively colder surface. Hence a reduction can be seen in the temperature profile.

Figs. 15−17 exhibit the variation of the permeability parameter $k^\star$ on the velocity $f'(\eta)$, temperature $\theta(\eta)$, and concentration $\varphi(\eta)$ fields, respectively. As the permeability parameter $k^\star$ increases, the flow velocity $f'(\eta)$, temperature $\theta(\eta)$, and concentration $\varphi(\eta)$ decrease for SWCNT and MWCNT. Since the permeability is proportional to the fluid's dynamic viscosity, its booming values retards the motion of the fluid. While the permeability is reversely proportional to the pressure difference, so for the increasing values of $k^\star$, the pressure difference decreases, resulting in the reduction in the temperature profile.

The impact of magnetic parameter Re_m on the velocity, temperature, and concentration are demonstrated in Figs. 18−20, respectively. The rising values of magnetic parameter Re_m lead to a decrease in the velocity, temperature, and concentration profiles for SWCNT and MWCNT nanofluid. The fluid flow becomes more convective along with the escalating values of the magnetic parameter also it is generated by the Lorentz force. The Lorentz force and convective flow produce resistance for the fluidic flow which causes the de-escalation of fluid velocity, temperature, and concentration. Fig. 21 demonstrates the impact of Brinkman number Br on the temperature profile $\theta(\eta)$. The enlargement of Brinkman number Br leads to an increment in temperature $\theta(\eta)$. For both SWCNT and MWCNT, the increment in temperature has happened, so the thermal boundary layer also increases for both nanofluids. Physically, it occurs because the booming values of Brinkman number Br result in more heat generation by viscous dissipation and slower conduction of heat; subsequently, the temperature $\theta(\eta)$ increases significantly.

The impact of heterogeneous parameter K_s on the concentration profile $\varphi(\eta)$ is demonstrated in Fig. 22. It is monitored that the booming values of heterogeneous parameter K_s lead to a fall off in the concentration profile $\varphi(\eta)$ for both SWCNT and MWCNT nanofluids. Since the heterogeneous parameter K_s is reversely proportional to the mass diffusivity, the booming values of K_s cause the reduction in mass diffusivity. Consequently, the decay can be seen in the concentration profile $\varphi(\eta)$.

The variations of the concentration distribution $\varphi(\eta)$ for the distinct values of Schmidt number Sc are manifested in Fig. 23. The concentration profile $\varphi(\eta)$ grows along with the enlarging values of Schmidt number Sc for both nanofluids. It is to be noted that the Schmidt number Sc is the ratio of momentum diffusivity to mass diffusivity. Hence, the mass diffusivity decreases along with the increasing values of the Schmidt number Sc, and as a result, the concentration distribution $\varphi(\eta)$ reduces.

Fig. 24 depicts the impact of homogeneous parameter K on the concentration profile $\varphi(\eta)$. It is discovered that the rise of homogeneous parameter K results in a reduction in the concentration profile $\varphi(\eta)$ for both nanofluids. As homogeneous parameter K increases, the mass diffusion rate decays which in turn slows down the transportation of mass species which results in de-escalation of the mass distribution.

Table III has demonstrated the effects of various parameters like m, $\alpha^\star$, A, ϕ, $k^\star$, Re_m, Br, K_s, Sc, and K on the wall shear stress $f''(0)$, wall heat flux $\theta'(0)$, and the rate of concentration $\varphi'(0)$, with keeping $Pr = 25$ fixed. From Eq. (26), the skin friction coefficient and the local Nusselt number are proportional to the surface shear stress $f''(0)$ and the surface heat flux $\theta'(0)$, respectively. It is observed that the increment in parameters m, $k^\star$, and Re_m leads to a reduction in surface shear stress $f''(0)$ but reverse results are found if parameters $\alpha^\star$, A, and ϕ are taken into account. The heat transfer rate grows along with the booming values of A and Br, while the opposite phenomenon arises for parameters m,

$\alpha^\star$, ϕ, $k^\star$, and Re_m. Furthermore, the incremental changes in parameters A, ϕ, K_s, and Sc cause the enlargement in the rate of concentration $\varphi'(0)$. The reversal behavior is seen for parameters m, $\alpha^\star$, $k^\star$, Re_m, and K. The MWCNT-blood nanofluid has higher surface shear stress $f''(0)$, surface heat flux $\theta'(0)$, and rate of concentration $\varphi'(0)$ when compared with SWCNT-blood nanofluid.

7 Conclusions

In this work, the numerical examination of the influence of homogeneous-heterogeneous chemical reaction on the electro-hydrodynamic flow of nanofluid over a porous non-linear stretching sheet has been carried out. The effect of Joule heating and viscous dissipation on heat transfer has been considered. The Galerkin finite element scheme has been used to find the numerical solution. The main concluding remarks from this work are as follows.

1. The velocity, temperature, concentration, surface shear stress, surface heat flux, and rate of concentration profiles for MWCNT-blood nanofluid are higher than SWCNT-blood nanofluid for all controlling parameters.

2. The velocity reduces for enhancing values of the power index parameter when $\eta < 1.5$ for both types of nanofluids. However, the opposite phenomenon occurs when $\eta \geq 1.5$. The temperature, surface shear stress, surface heat flux, and rate of concentration decrease, while the concentration profile increases for both nanofluids.

3. There is a decrease in temperature, concentration, surface heat flux, and concentration rate as the wall thickness parameter is enhanced whereas the velocity and surface shear stress show opposite behavior for both nanofluids.

4. Velocity, temperature, concentration, surface shear stress, surface heat flux, and rate of concentration increase along with the increment in ratio parameter.

5. Velocity, concentration, surface shear stress, and rate of concentration are enhanced when the volume fraction parameter increases, but the temperature and surface heat flux decrease.

6. Enlargement in permeability parameter and magnetic parameter are results of reduction in the velocity, temperature, concentration, surface shear stress, surface heat flux, and rate of concentration profiles for SWCNT and MWCNT nanofluids.

7. The thermal boundary layer thickness and surface heat flux enhance along with the booming values of the Brinkman number.

8. Concentration profile declines while the concentration rate rises, corresponding to the rising values of the heterogeneous and homogeneous parameters whereas the opposite behavior can be seen for the Schimdt number.

Incorporating the Darcy-Forchheimer porous medium, inclined surface, adding hybrid nanofluids with different shapes, or calculating entropy generation could be the possible direction of future research.

Acknowledgements

Ajay Singh (09/964(0014)/2018-EMR-I) is grateful to CSIR, New Delhi, India, for financial favor in the form of Senior Research Fellowship.

References

[1] A. Mahdy, Unsteady mixed convection boundary layer flow and heat transfer of nanofluids due to stretching sheet, Nuclear Engineering and Design, 249, 248–255, (2012).

[2] A. Noghrehabadi, R. Pourrajab, M. Ghalambaz, Flow and heat transfer of nanofluids over stretching sheet taking into account partial slip and thermal convective boundary conditions, Heat and Mass Transfer, 49 (9), 1357–1366, (2013).

[3] Asma Khalid, Ilyas Khan, Arshad Khan, Sharidan Shafie, I. Tlili, Case study of MHD blood flow in a porous medium with CNTS and thermal analysis, Case Studies in Thermal Engineering, 12, 374–380, (2018).

[4] B. Jalilpour, S. Jafarmadar, D.D. Ganji, A.B. Shotorban, H. Taghavifar, Heat generation/absorption on MHD stagnation flow of nanofluid towards a porous stretching sheet with prescribed surface heat flux, Journal of Molecular Liquids, 195, 194–204 (2014).

[5] B. Mahanthesh, B.J. Gireesha, N.S. Shashikumar, S.A. Shehzad, Marangoni convective MHD flow of SWCNT and MWCNT nanoliquids due to a disk with solar radiation and irregular heat source, Physica E 94, 25–30, (2017).

[6] B.J. Gireesha, G.K. Ramesh, M.S. Abel, C.S. Bagewadi, Boundary layer flow and heat transfer of a dusty fluid flow over a stretching sheet with non-uniform heat source/sink, International Journal of Multiphase Flow, 37, 977–982, (2011).

[7] C. Bozkaya, M. Tezer-Sezgin, Fundamental solution for coupled magnetohydrodynamic flow equations, Journal of Computational and Applied Mathematics, 203, 125–144 (2007).

[8] D. Wen, Y. Ding, Effective thermal conductivity of aqueous suspensions of carbon nanotubes (Carbon Nanotube Nanofluids), Journal of Thermophysics and Heat Transfer, 18 (4), 481–485, (2004).

[9] K.L. Hsiao, Stagnation electrical MHD nanofluid mixed convection with slip boundary on a stretching sheet, Applied Thermal Engineering, 98, 850–861, (2016).

[10] L. Kumar, Finite element analysis of combined heat and mass transfer in hydromagnetic micropolar flow along a stretching sheet, Computational Materials Science, 46, 841–848, (2009).

[11] L. Wang, Q. Ni, M. Li, Q. Qian, The thermal effect on vibration and instability of carbon nanotubes conveying fluid, Physica E, 40, 3179–3182, (2008).

[12] L. Wang, Wave propagation of fluid-conveying single-walled carbon nanotubes via gradient elasticity theory, Computational Materials Science, 49, 761–766, (2010).

[13] L.J. Crane, Flow past a Stretching Plate, Journal of Applied Mathematics and Physics 21, 645–647, (1970).

[14] M. Ghalandari, E.M. Koohshahi, F. Mohamadian, S. Shamshirband, K.W. Chau, Numerical simulation of nanofluid flow inside a root canal, Engineering Applications of Computational Fluid Mechanics, 13 (1), 254–264, (2019).

[15] M. Sheikholeslami, D.D. Ganji, M.Y. Javed, R. Ellahi, Effect of thermal radiation on magnetohydrodynamics nanofluid flow and heat transfer by means of two phase model, Journal of Magnetism and Magnetic Materials, 374, 36–43, (2015).

[16] M. Turkyilmazoglu, Performance of direct absorption solar collector with nanofluid mixture, Energy Conversion and Management, 114, 1–10, (2016).

[17] M. Turkyilmazoglu, Thermal radiation effects on the time-dependent MHD permeable flow having variable viscosity, International Journal of Thermal Sciences, 50, 88–96, (2011).

[18] M. Whitby, N. Quirke, Fluid flow in carbon nanotubes and nanopipes, Nature Nanotechnology, 2 (2), 87–94, (2007).

[19] M.A. Ahmed, N.H. Shuaib, M.Z. Yusoff, A.H. Al-Falahi, Numerical investigations of flow and heat transfer enhancement in a corrugated channel using nanofluid, International Communications in Heat and Mass Transfer, 38, 1368–1375, (2011).

[20] M.M. Rashidi, M. Reza, S. Gupta, MHD stagnation point flow of micropolar nanofluid between parallel porous plates with uniform blowing, Powder Technology, 301, 876–885, (2016).

[21] M.M. Rashidi, N.V. Ganesh, A.K.A. Hakeem, B. Ganga, Buoyancy effect on MHD flow of nanofluid over a stretching sheet in the presence of thermal radiation, Journal of Molecular Liquids, 198, 234–238, (2014).

[22] N. Bachok, A. Ishak, I. Pop, Boundary-layer flow of nanofluids over a moving surface in a flowing fluid, International Journal of Thermal Sciences, 49, 1663–1668, (2010).

[23] N. Bachok, A. Ishak, I. Pop, Melting heat transfer in boundary layer stagnation-point flow towards a stretching/shrinking sheet, Physics Letters A, 374, 4075–4079, (2010).

[24] N.F.M. Noor, R.U. Haq, S. Nadeem, I. Hashim, Mixed convection stagnation flow of a micropolar nanofluid along a vertically stretching surface with slip effects, Meccanica, 50 (8), 2007–2022, (2015).

[25] P.A. Davidson, An introduction to Magnetohydrodynamics, Cambridge University Press (2001).

[26] R. Ellahi, The effects of MHD and temperature dependent viscosity on the flow of non-Newtonian nanofluid in a pipe: Analytical solutions, Applied Mathematical Modelling, 37, 1451–1467, (2013).

[27] R. Jain, R. Mehta, T. Mehta, J. Singh, D. Baleanu, MHD flow and heat and mass transport investigation over a decelerating disk with Ohmic heating and diffusive effect, Thermal Science, 27, 141–149, (2023).

[28] R. Kumar, J. Singh, R. Mehta, D. Kumar, D. Baleanu, Analysis of the impact of thermal radiation and velocity slip on the melting of magnetic hydrodynamic micropolar fluid-flow over an exponentially stretching sheet, Thermal Science, 27, 311–322, (2023).

[29] R. Mehta, R. Kumar, H. Rathore, J. Singh, Joule heating effect on radiating MHD mixed convection stagnation point flow along vertical stretching sheet embedded in a permeable medium and heat generation/absorption, Heat Transfer (Wiley), 51, 7369–7386, (2022).

[30] S. Chaudhary, Analysis of Cu water nanofluid flow with different particle shapes over an isothermal moving plate, Indian Journal of Chemical Technology, 29, 311–317, (2022).

[31] S. Chaudhary, K.K. Chouhan, Darcy-Forchheimer flow of Prandtl-Eyring nanofluid subjected to a Riga plate of varying thickness along with Brownian diffusion, thermophoresis and non-uniform heat source/sink effects, Numerical Heat Transfer, Part A: Applications, 84, 732–759, (2023).

[32] S. Chaudhary, KM Kanika, M.K. Choudhary, Newtonian heating and convective boundary condition on MHD stagnation point flow past a stretching sheet with viscous disipation and joule heating, Indian Journal of Pure and Applied Physics, 56, 931–940, (2018).

[33] S. Chaudhary, KM Kanika, Radiation heat transfer on SWCNT and MWCNT based magnetohydrodynamic nanofluid flow with Marangoni convection, Physica Scripta, 95 (2) (2019).

[34] S. Chaudhary, KM Kanika, Viscous dissipation and Joule heating in MHD Marangoni boundary layer flow and radiation heat transfer of Cu-water nanofluid along particle shapes over an exponential temperature, International Journal of Computer Mathematics, 97 (5), 943–958, (2020).

[35] S. Chaudhary, M.K. Choudhary, Partial slip and thermal radiation effects on hydromagnetic flow Over an exponentially stretching surface with suction or blowing, Thermal Science, 22 (2), 797–808, (2018).

[36] S. Jangid, R. Mehta, J. Singh, D. Baleanu, A.S. Alshomrani, Heat and mass transport of hydromagnetic williamson nanofluid passing through a permeable media across an extended sheet of varying thickness, Thermal Science, 27, 141-149, (2023).

[37] S. Lijima, Helical microtubules of graphitic carbon, Nature, 354, 56–58, (1991).

[38] S.-Q. Zhou, R. Ni, Measurement of the specific heat capacity of water-based Al_2O_3 nanofluid, Applied Physics Letters, 92 (9), 093123, (2008).

[39] S.A. Shehzad, T. Hayat, A. Alsaedi, Influence of convective heat and mass conditions in MHD flow of nanofluid, Bulletin of the Polish Academy of Sciences-Technical Sciences, 63, 465–474, (2015).

[40] S.U.S. Choi, J.A. Eastman, Enhancing thermal conductivity of fluids with nanoparticles, Publ. Fed 231ASME, 99–106, (1995).

[41] T. Hayat, Zakir Hussain, A. Alsaedi, S. Asghar, Carbon nanotubes effects in the stagnation point flow towards a nonlinear stretching sheet with variable thickness, Advanced Powder Technology, 27, 1677–1688, (2016).

[42] T.R. Mahapatra, A.S. Gupta, Heat transfer in stagnation-point flow towards a stretching sheet, Heat and mass transfer, 38, 517–521, (2002).

[43] W.A. Khan, Z.H. Khan, M. Rahi, Fluid flow and heat transfer of carbon nanotubes along a flat plate with Navier slip boundary, Applied Nanoscience, 4 (5), 633–641, (2013).

[44] Y. Ding, H. Alias, D. Wen, R.A. Williams, Heat transfer of aqueous suspensions of carbon nanotubes (CNT nanofluids), International Journal of Heat and Mass Transfer, 49, 240-250, (2006).

Table I: Thermophysical properties of used materials

Properties	Human Blood	SWCNT	MWCNT
$\rho(Kg/m^3)$	1053	2600	1600
$\sigma_e(S/m)$	0.8	$10^6 - 10^7$	1.9×10^{-4}
$C_p(J/KgK)$	3594	425	796
$\kappa(W/mK)$	0.492	6600	3000

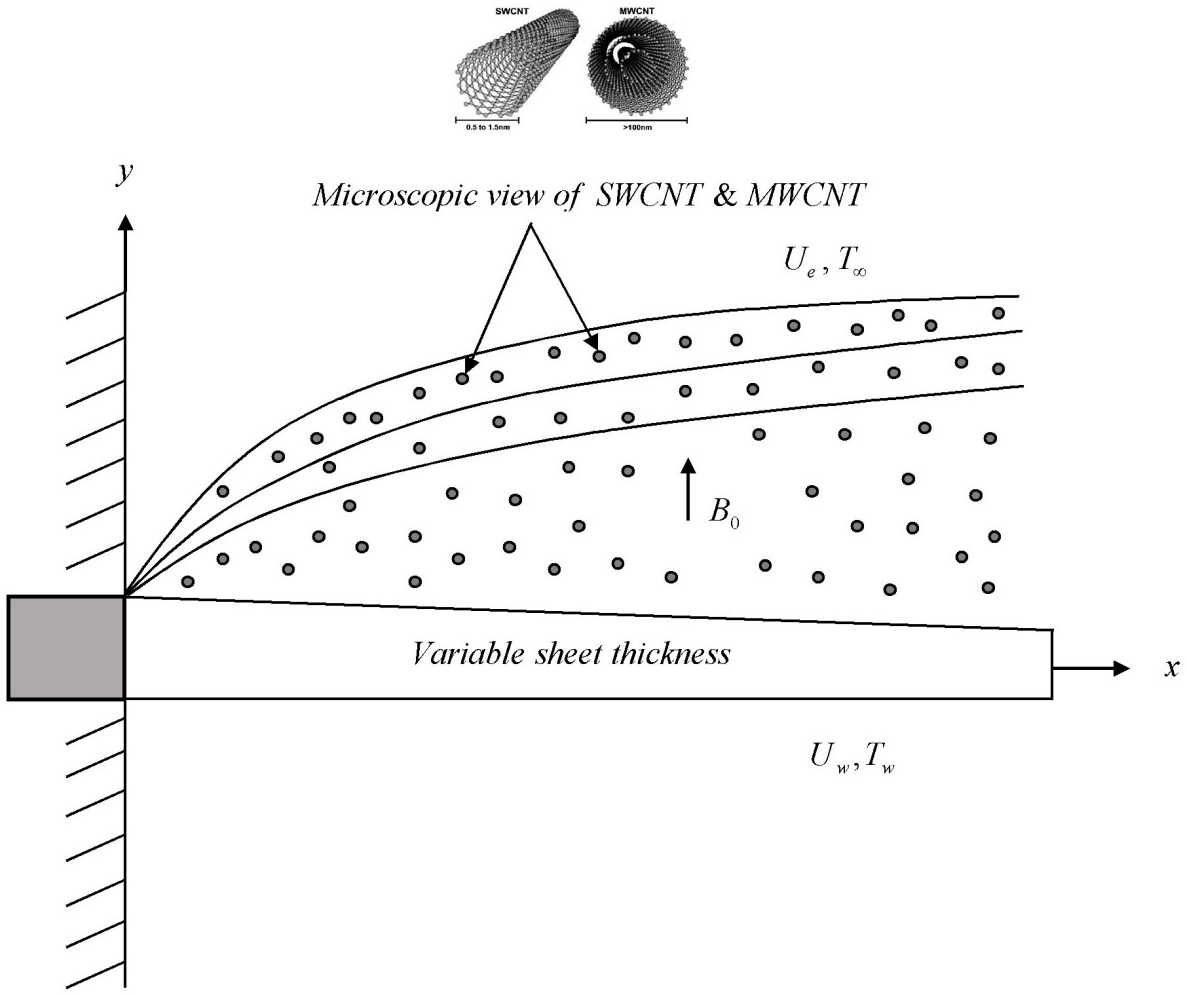

Figure 1: Sketch of the physical problem

Table II: Comparison of $-f''(0)$ with previously data when $m = 1$, $\alpha^\star =$ may have any value, $\phi = 0$, $Re_m = 0$

A	$k^\star$	Hayat et al. [2016]	Present results
0.1	0.0	0.969379	0.969436
0.2		0.918106	0.918113
0.5		0.667262	0.667264
0.0	0.5	1.2247	1.224776
	1.0	1.4142	1.414216
	1.5	1.5811	1.581139
	2.0	1.7320	1.732051
	5.0	2.4494	2.449490

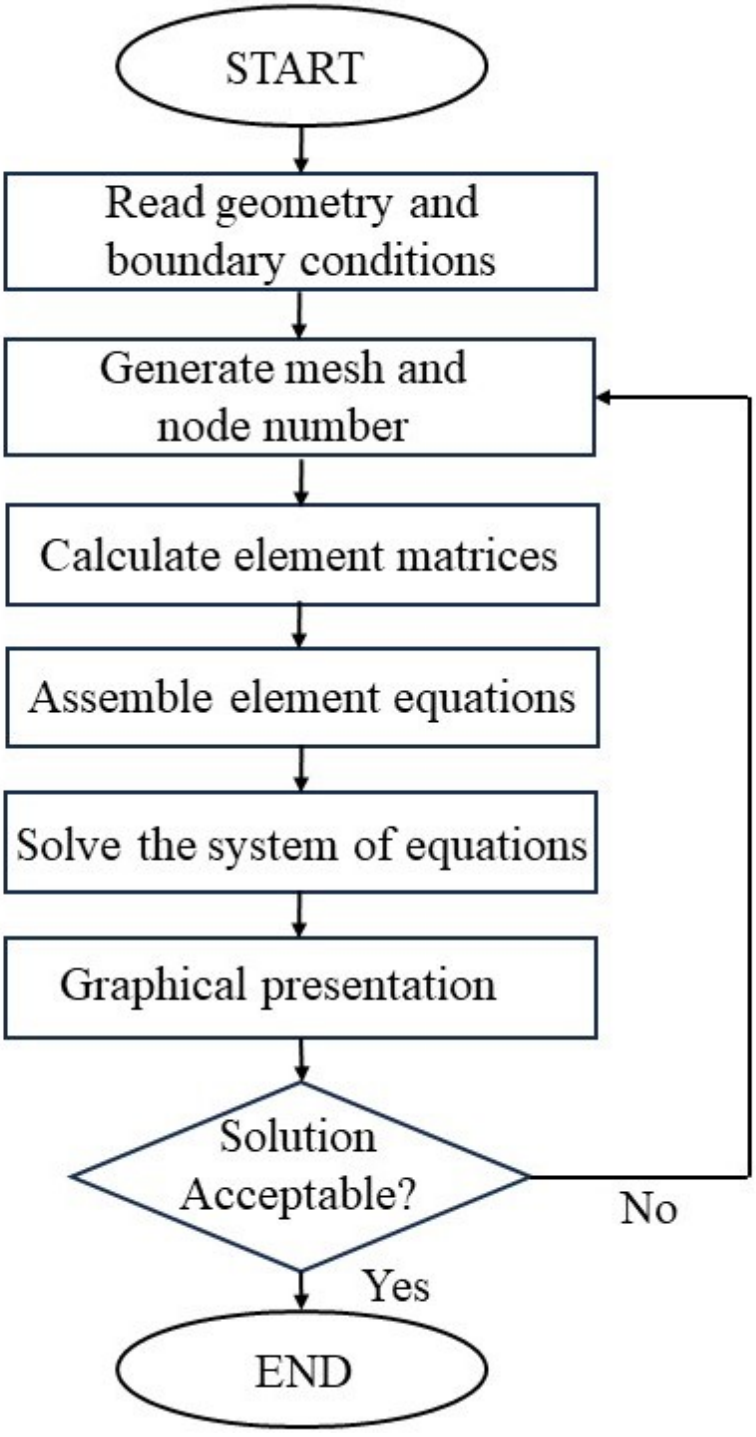

Figure 2: Flow chart of Galerkin finite element scheme

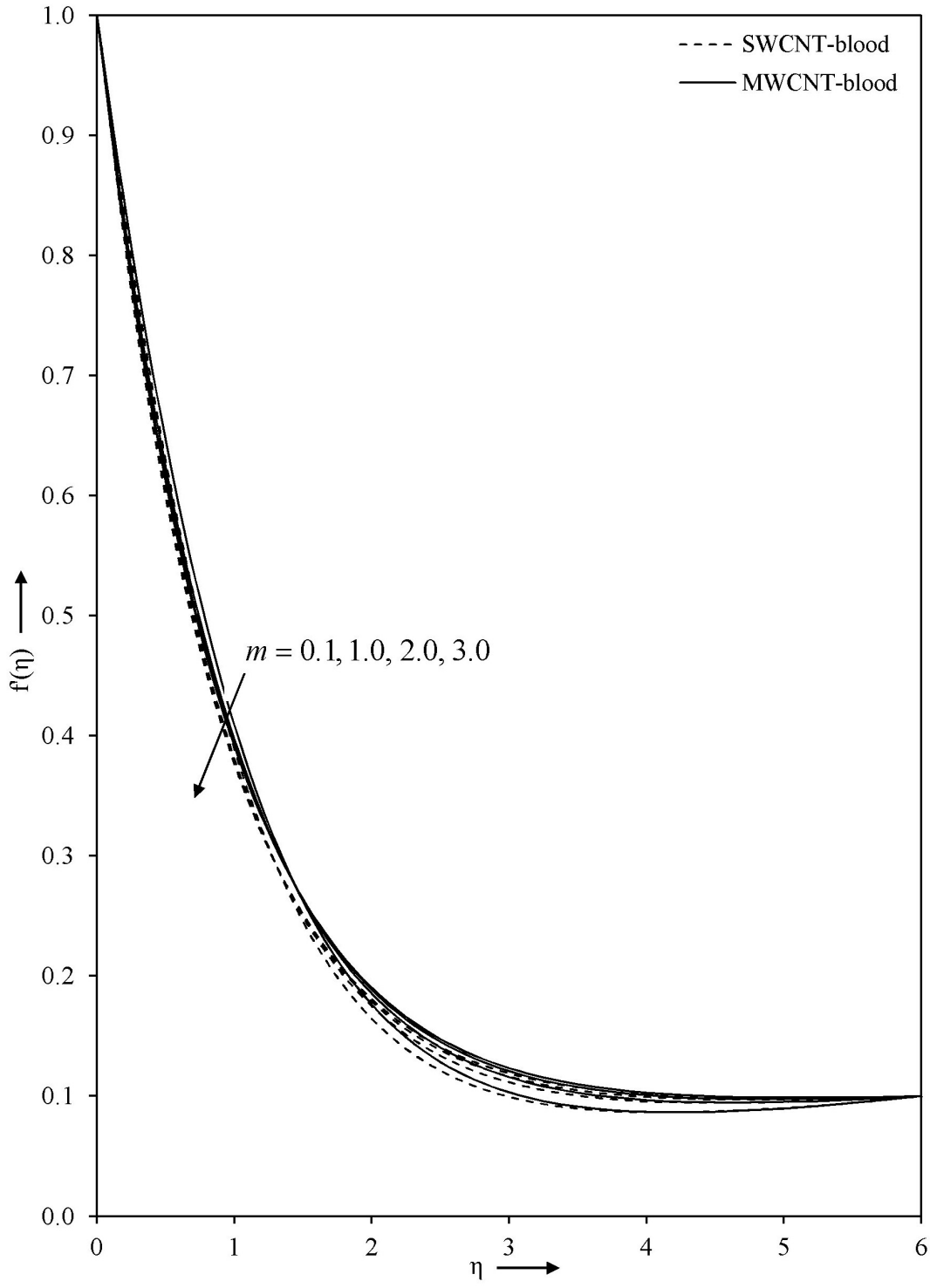

Figure 3: Impact of power index parameter m on velocity profile with $\alpha^\star = 0.1$, $A = 0.1$, $\phi = 0.1$, $k^\star = 0.1$ and $Re_m = 0.1$

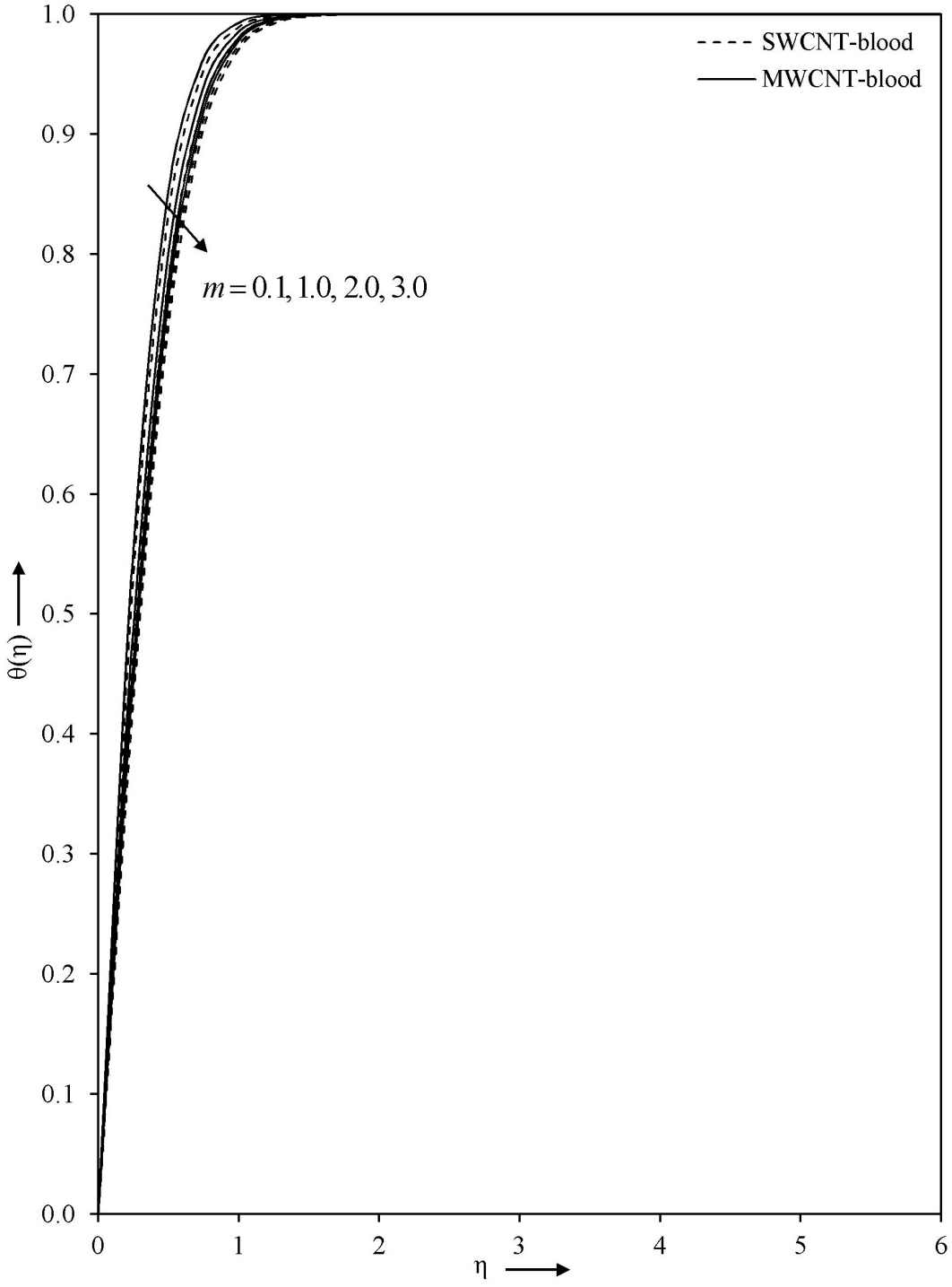

Figure 4: Impact of power index parameter m on temperature profile with $\alpha^{\star} = 0.1$, $A = 0.1$, $\phi = 0.1$, $k^{\star} = 0.1$, $Re_m = 0.1$, $Pr = 25$ and $Br = 0.1$

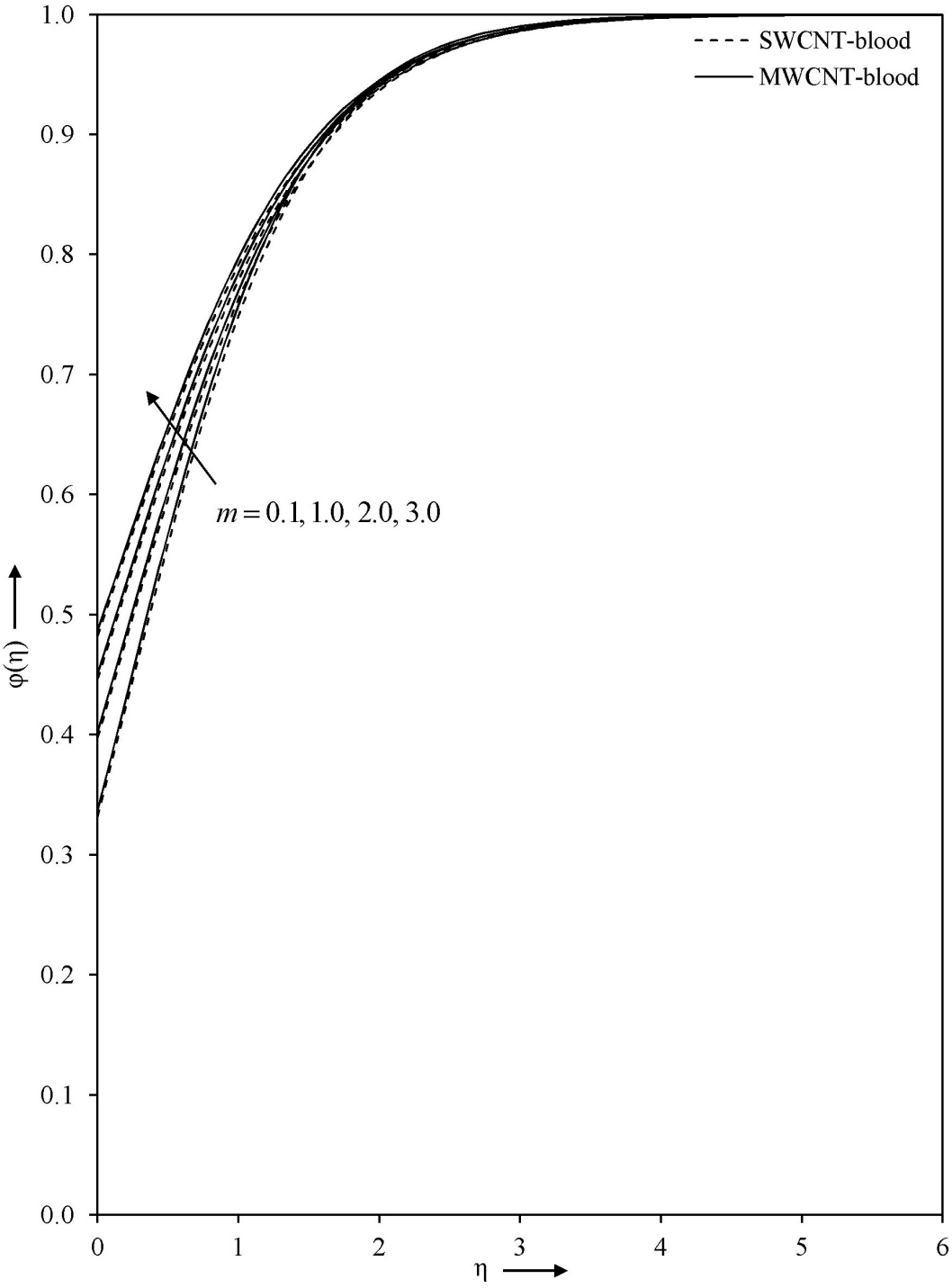

Figure 5: Impact of power index parameter m on concentration profile with $\alpha^{\star} = 0.1$, $A = 0.1$, $\phi = 0.1$, $k^{\star} = 0.1$, $Re_m = 0.1$, $K_s = 1.0$, $Sc = 1.5$ and $K = 0.5$

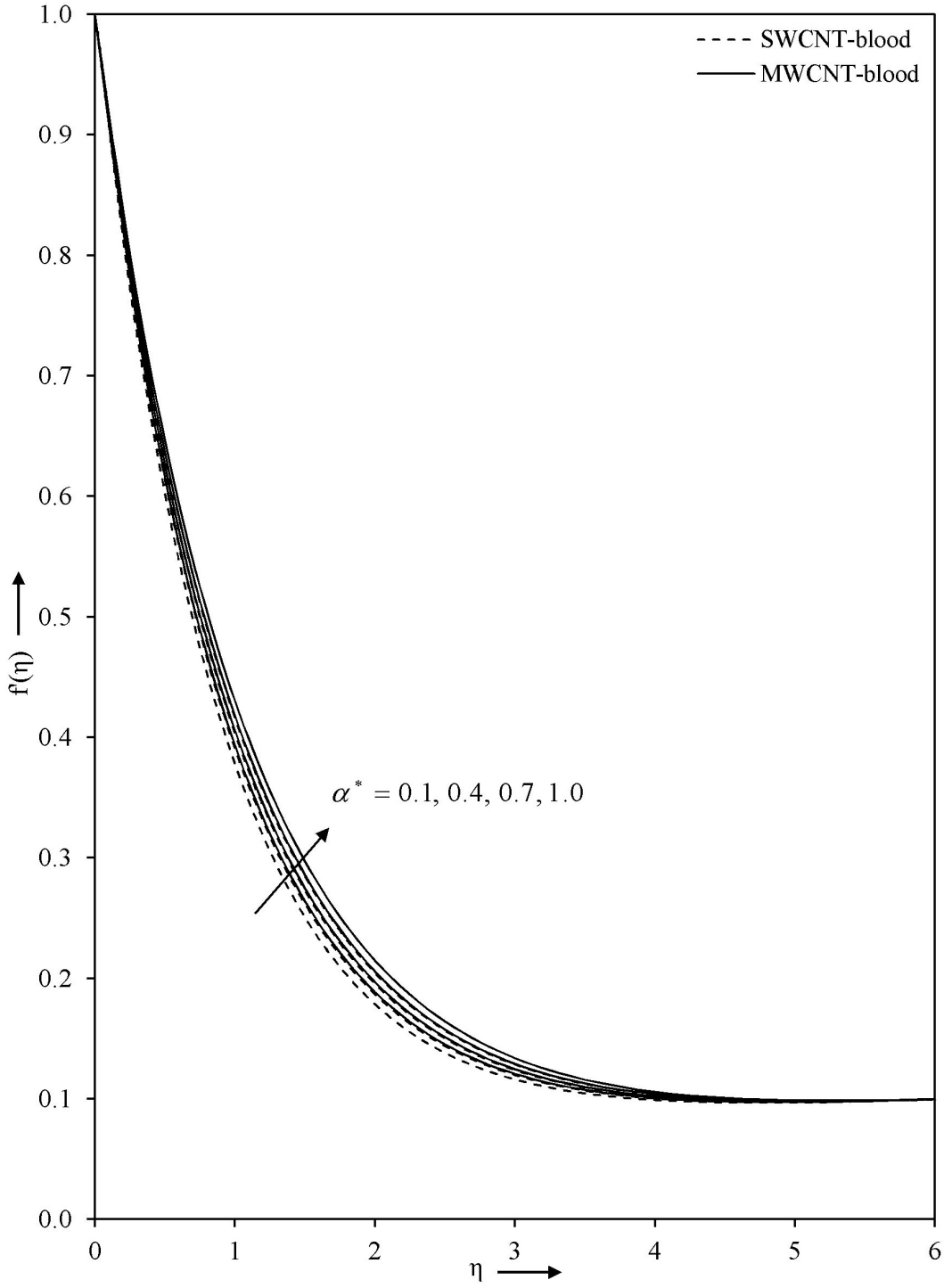

Figure 6: Impact of wall thickness parameter $\alpha^\star$ on velocity profile with $m = 2.0$, $A = 0.1$, $\phi = 0.1$, $k^\star = 0.1$ and $Re_m = 0.1$

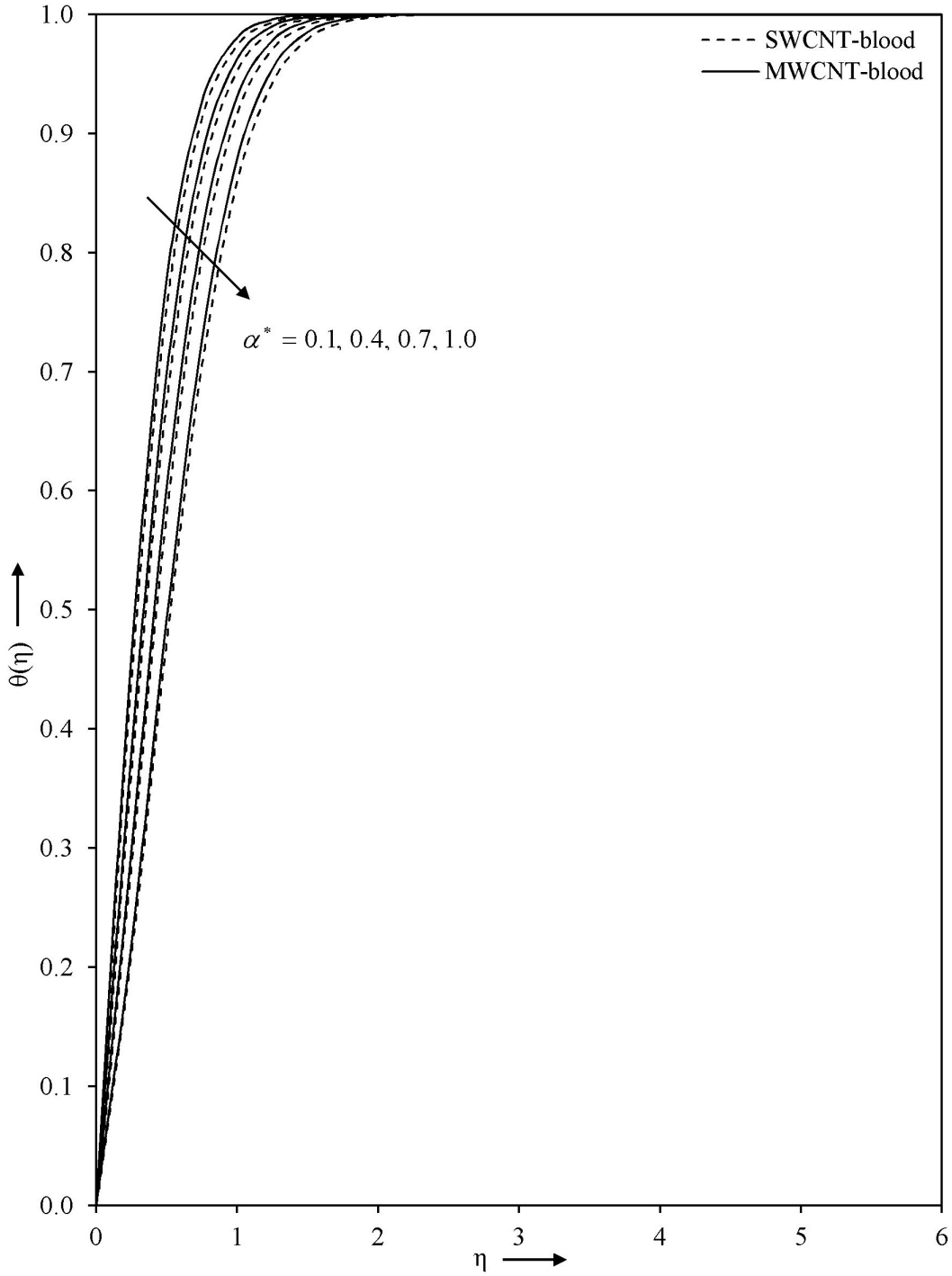

Figure 7: Impact of wall thickness parameter $\alpha^\star$ on temperature profile with $m = 2.0$, $A = 0.1$, $\phi = 0.1$, $k^\star = 0.1$, $Re_m = 0.1$, $Pr = 25$ and $Br = 0.1$

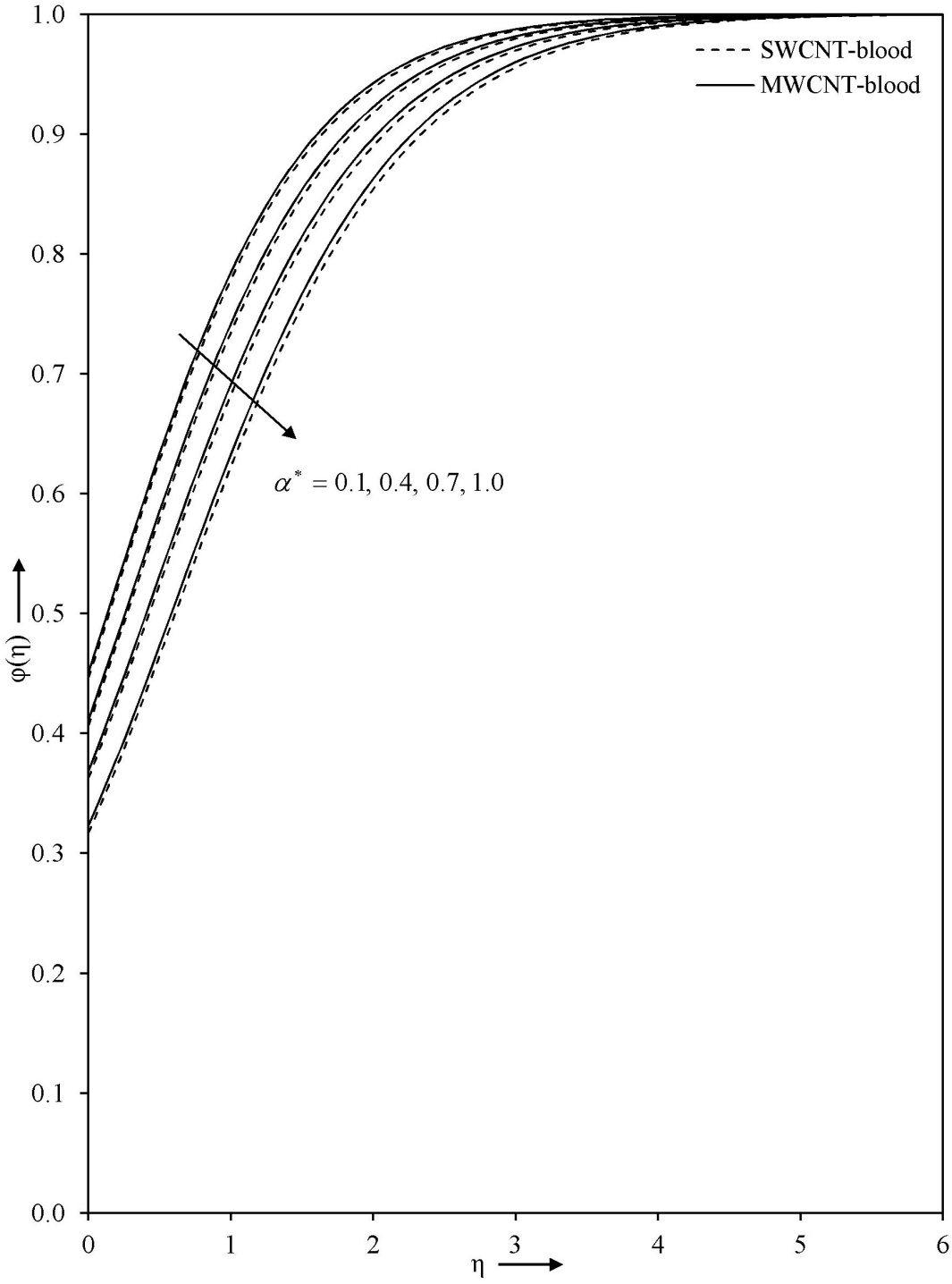

Figure 8: Impact of wall thickness parameter $\alpha^\star$ on concentration profile with $m = 2.0$, $A = 0.1$, $\phi = 0.1$, $k^\star = 0.1$, $Re_m = 0.1$, $K_s = 1.0$, $Sc = 1.5$ and $K = 0.5$

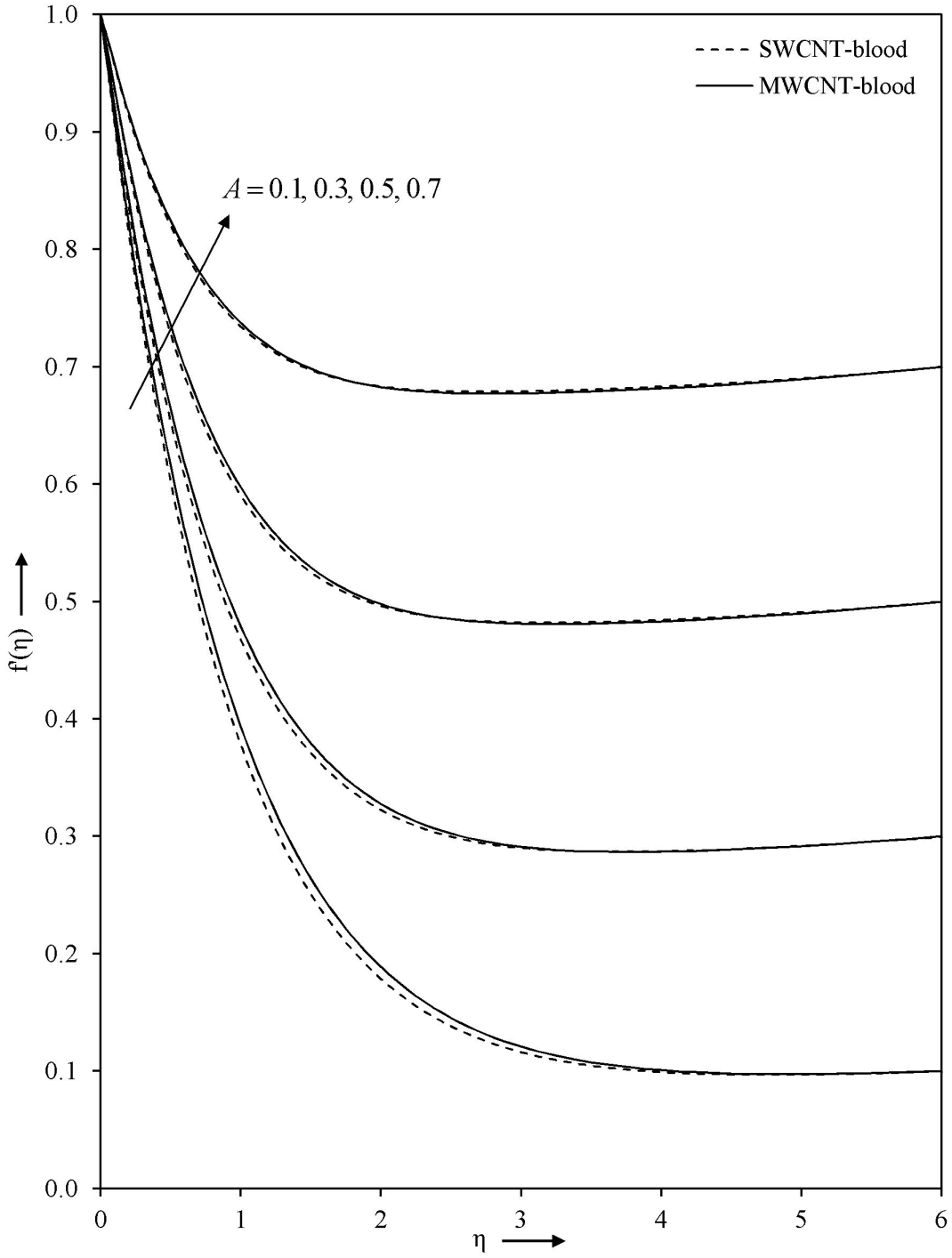

Figure 9: Impact of ratio parameter A on velocity profile with $m = 2.0$, $\alpha^{\star} = 0.1$, $\phi = 0.1$, $k^{\star} = 0.1$ and $Re_m = 0.1$

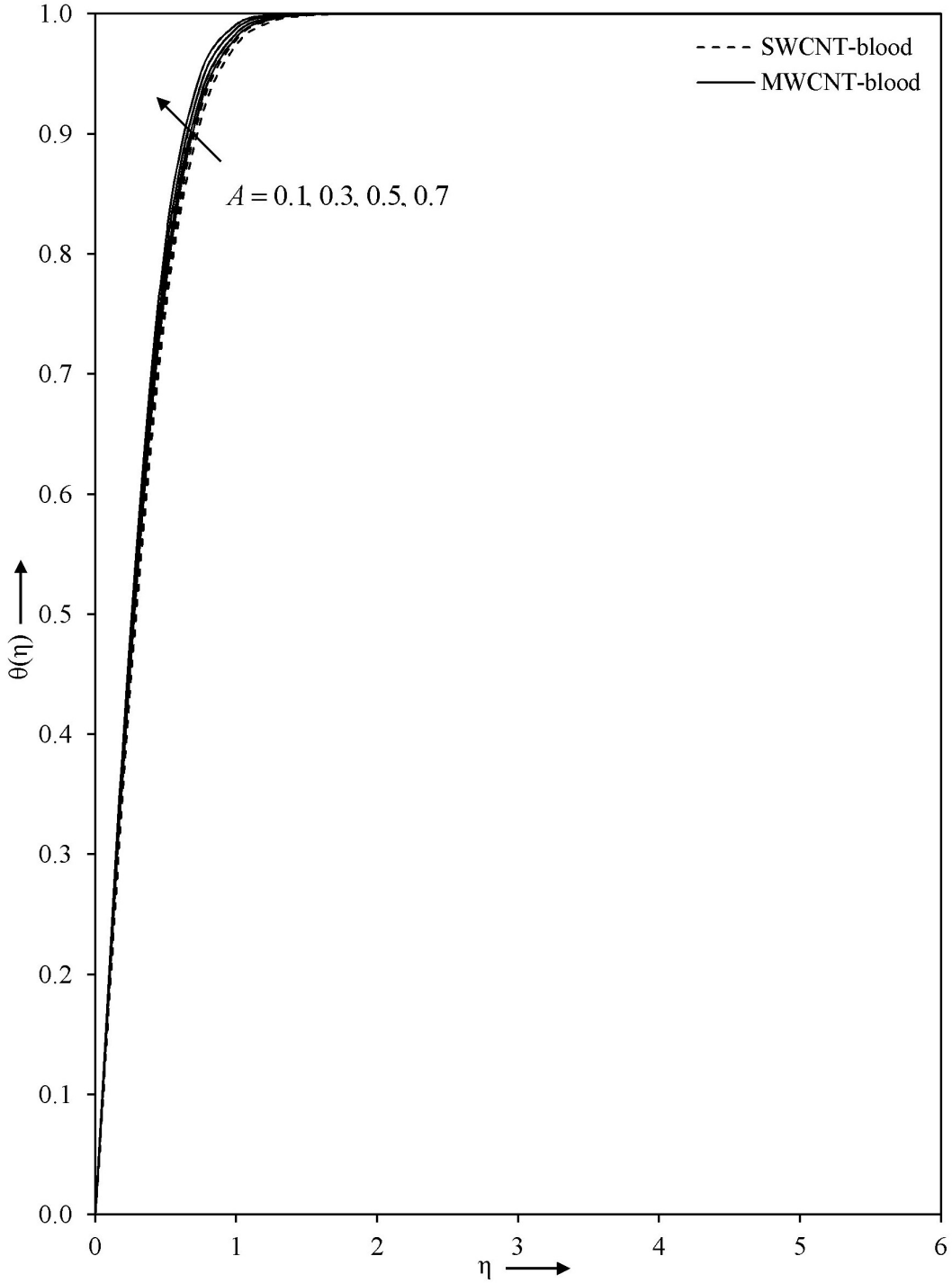

Figure 10: Impact of ratio parameter A on temperature profile with $m = 2.0$, $\alpha^{\star} = 0.1$, $\phi = 0.1$, $k^{\star} = 0.1$, $Re_m = 0.1$, $Pr = 25$ and $Br = 0.1$

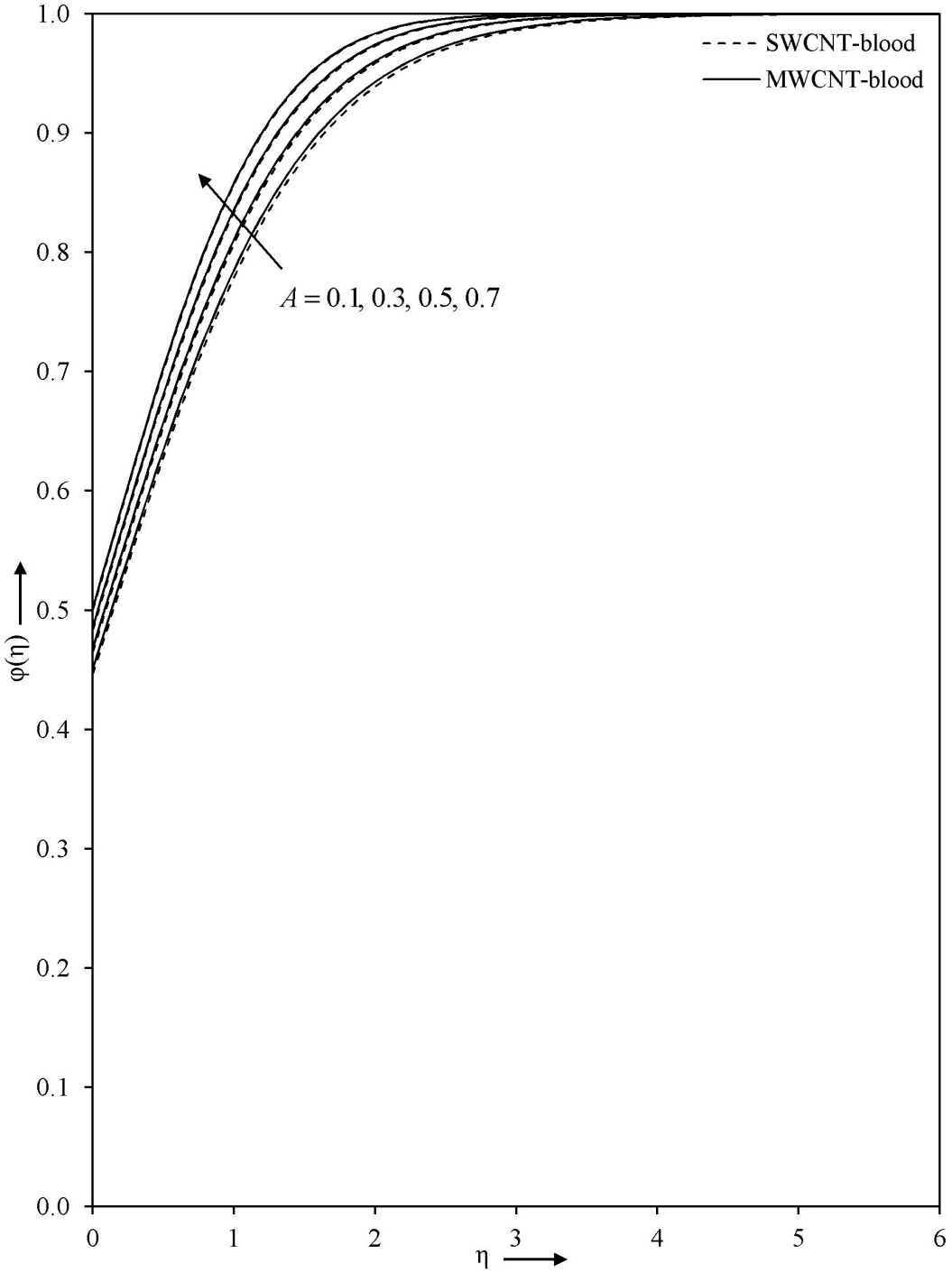

Figure 11: Impact of ratio parameter A on concentration profile with $m = 2.0$, $\alpha^{\star} = 0.1$, $\phi = 0.1$, $k^{\star} = 0.1$, $Re_m = 0.1$, $K_s = 1.0$, $Sc = 1.5$ and $K = 0.5$

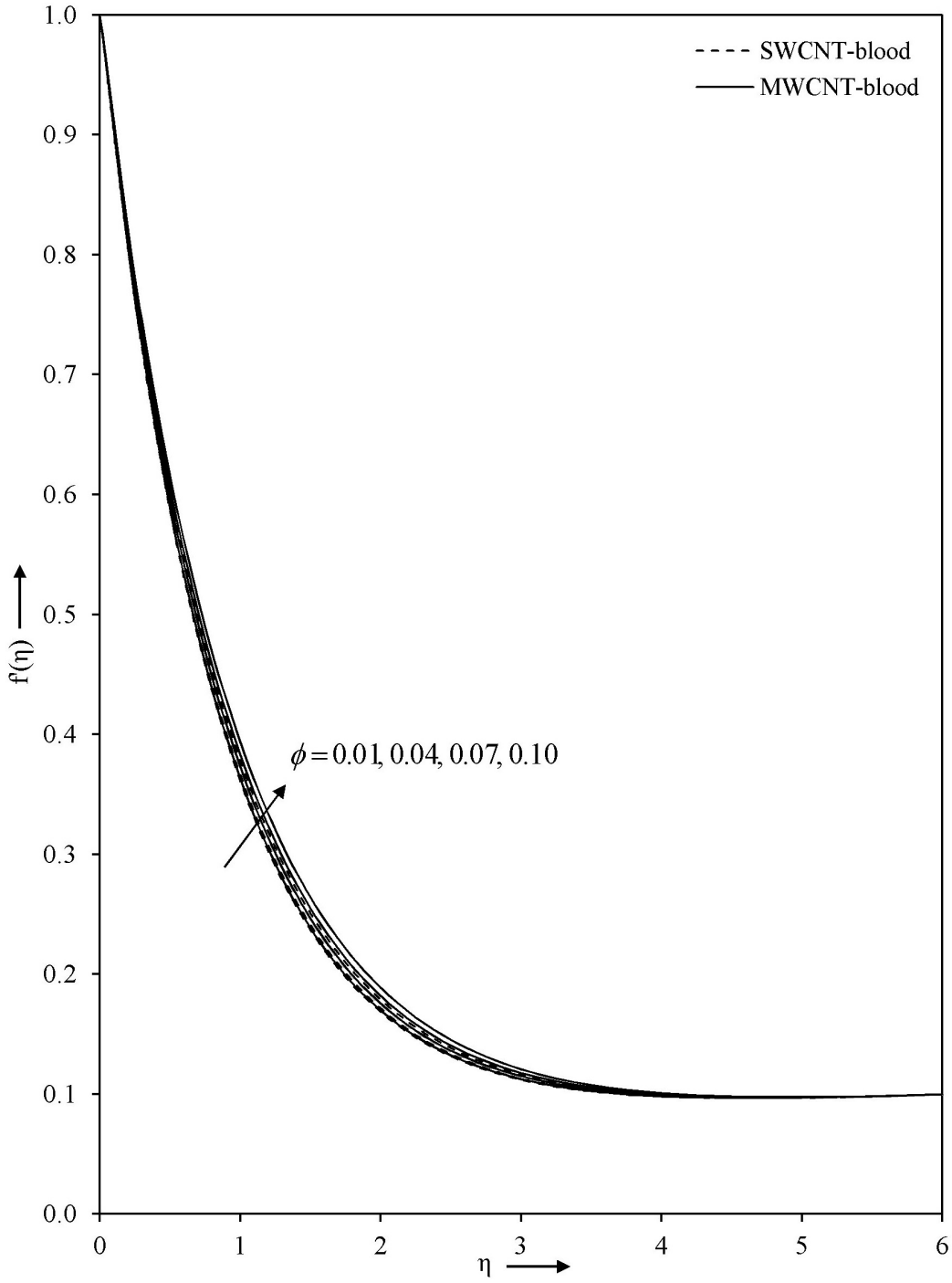

Figure 12: Impact of volume fraction parameter ϕ on velocity profile with $m = 2.0$, $\alpha^\star = 0.1$, $A = 0.1$, $k^\star = 0.1$ and $Re_m = 0.1$

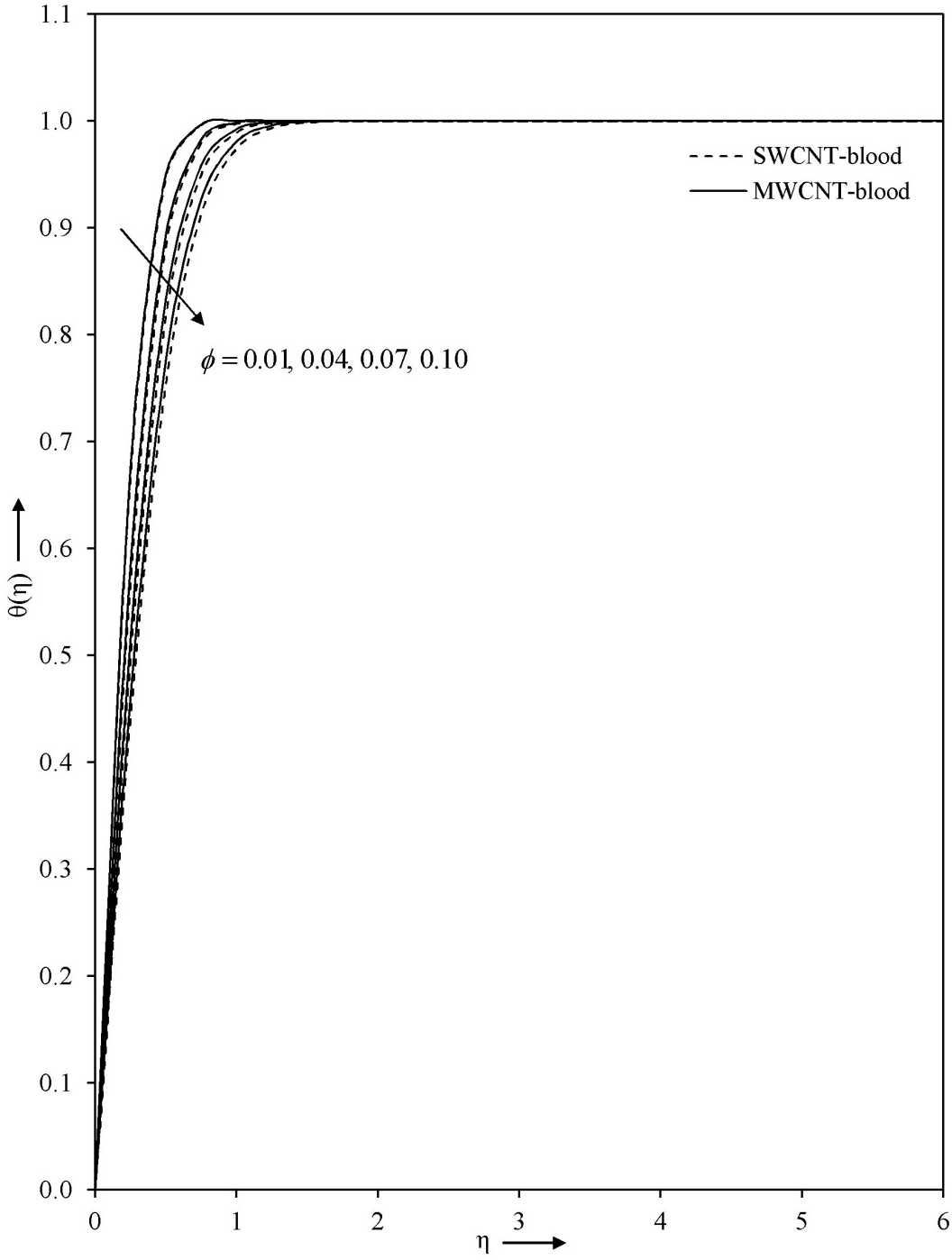

Figure 13: Impact of volume fraction parameter ϕ on temperature profile with $m = 2.0$, $\alpha^{\star} = 0.1$, $A = 0.1$, $k^{\star} = 0.1$, $Re_m = 0.1$, $Pr = 25$ and $Br = 0.1$

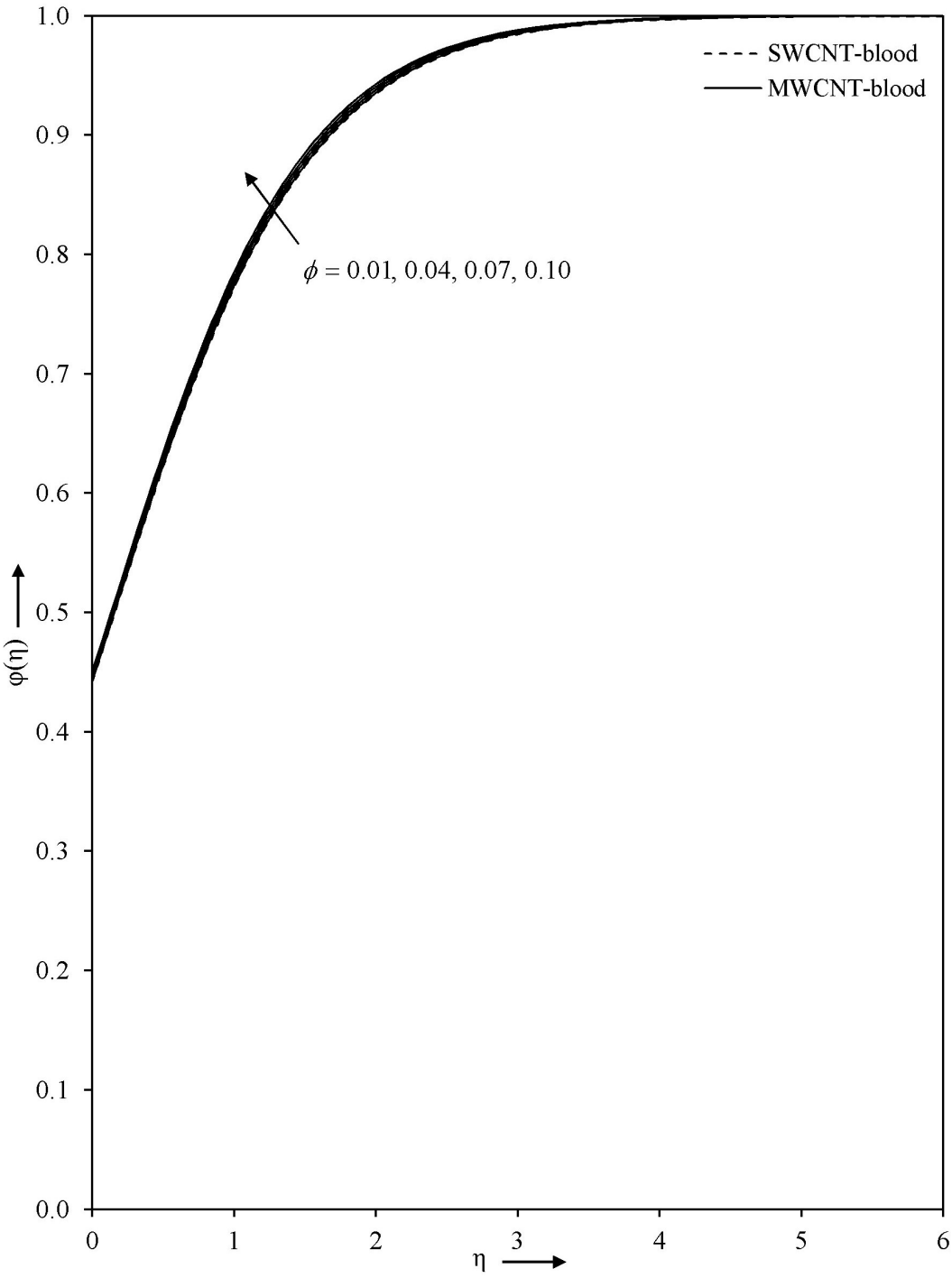

Figure 14: Impact of volume fraction parameter ϕ on concentration profile with $m = 2.0$, $\alpha^{\star} = 0.1$, $A = 0.1$, $k^{\star} = 0.1$, $Re_m = 0.1$, $K_s = 1.0$, $Sc = 1.5$ and $K = 0.5$

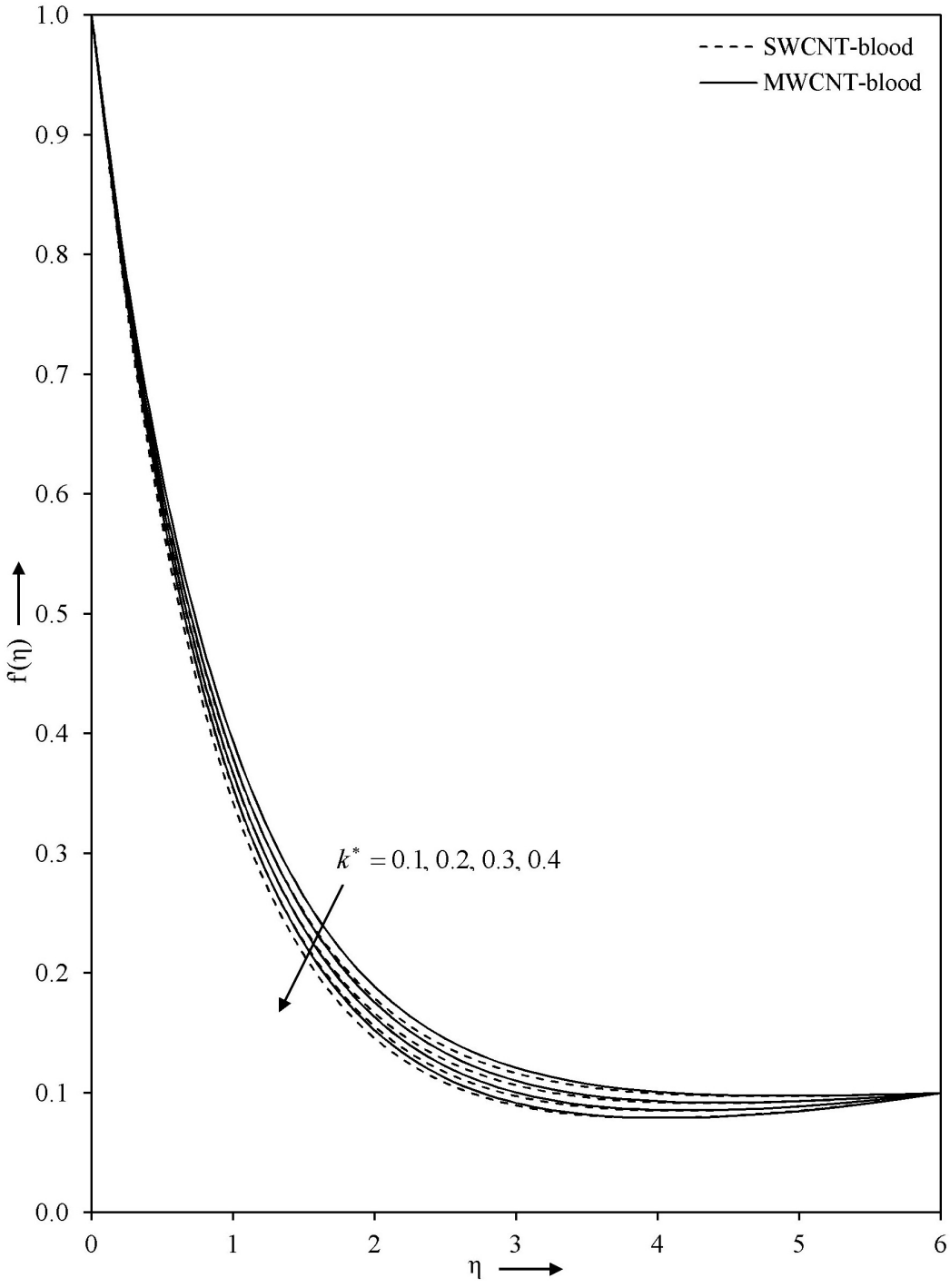

Figure 15: Impact of permeability parameter $k^\star$ on velocity profile with $m = 2.0$, $\alpha^\star = 0.1$, $A = 0.1$, $\phi = 0.1$ and $Re_m = 0.1$

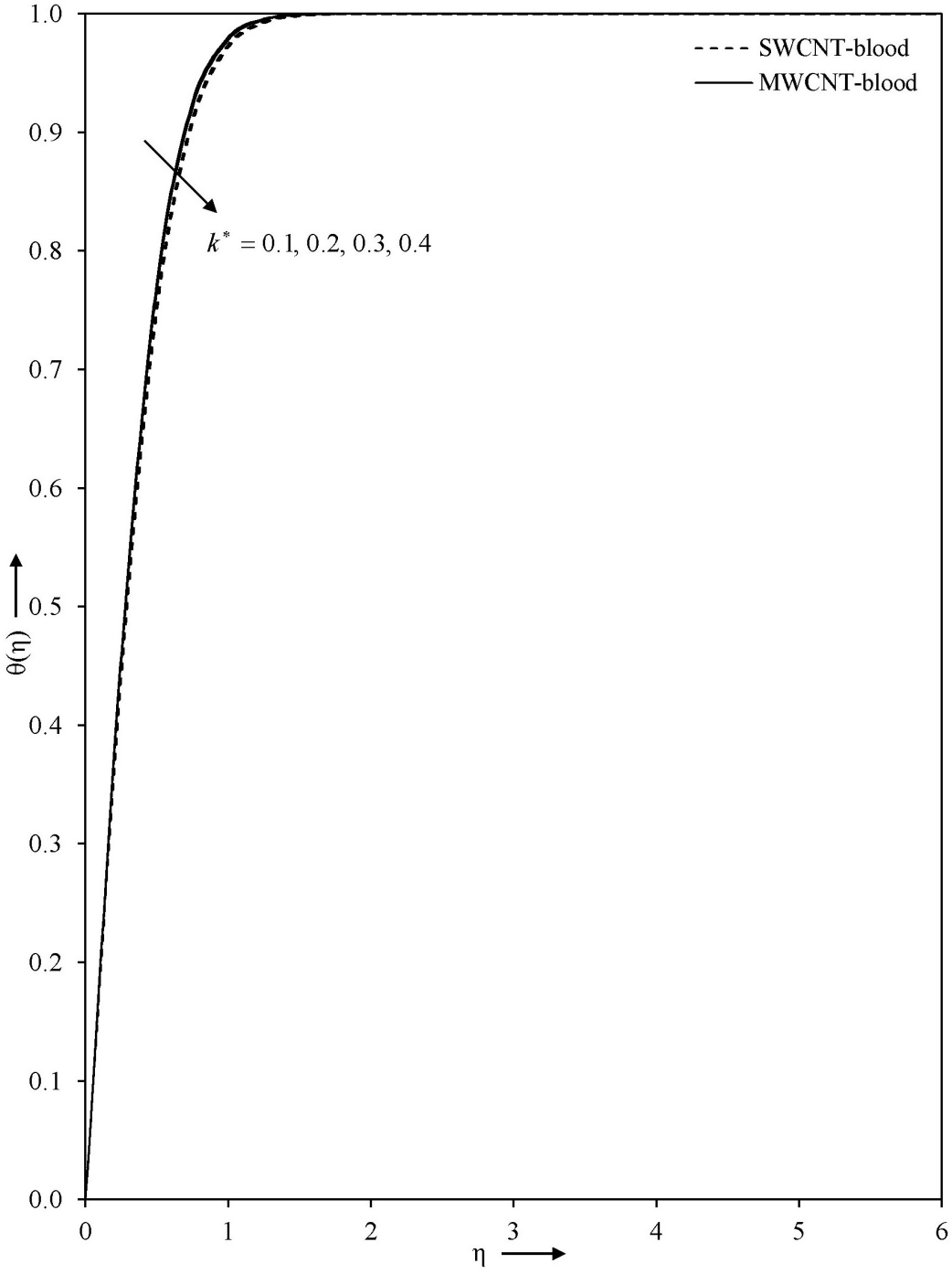

Figure 16: Impact of permeability parameter $k^\star$ on temperature profile with $m = 2.0$, $\alpha^\star = 0.1$, $A = 0.1$, $\phi = 0.1$, $Re_m = 0.1$, $Pr = 25$ and $Br = 0.1$

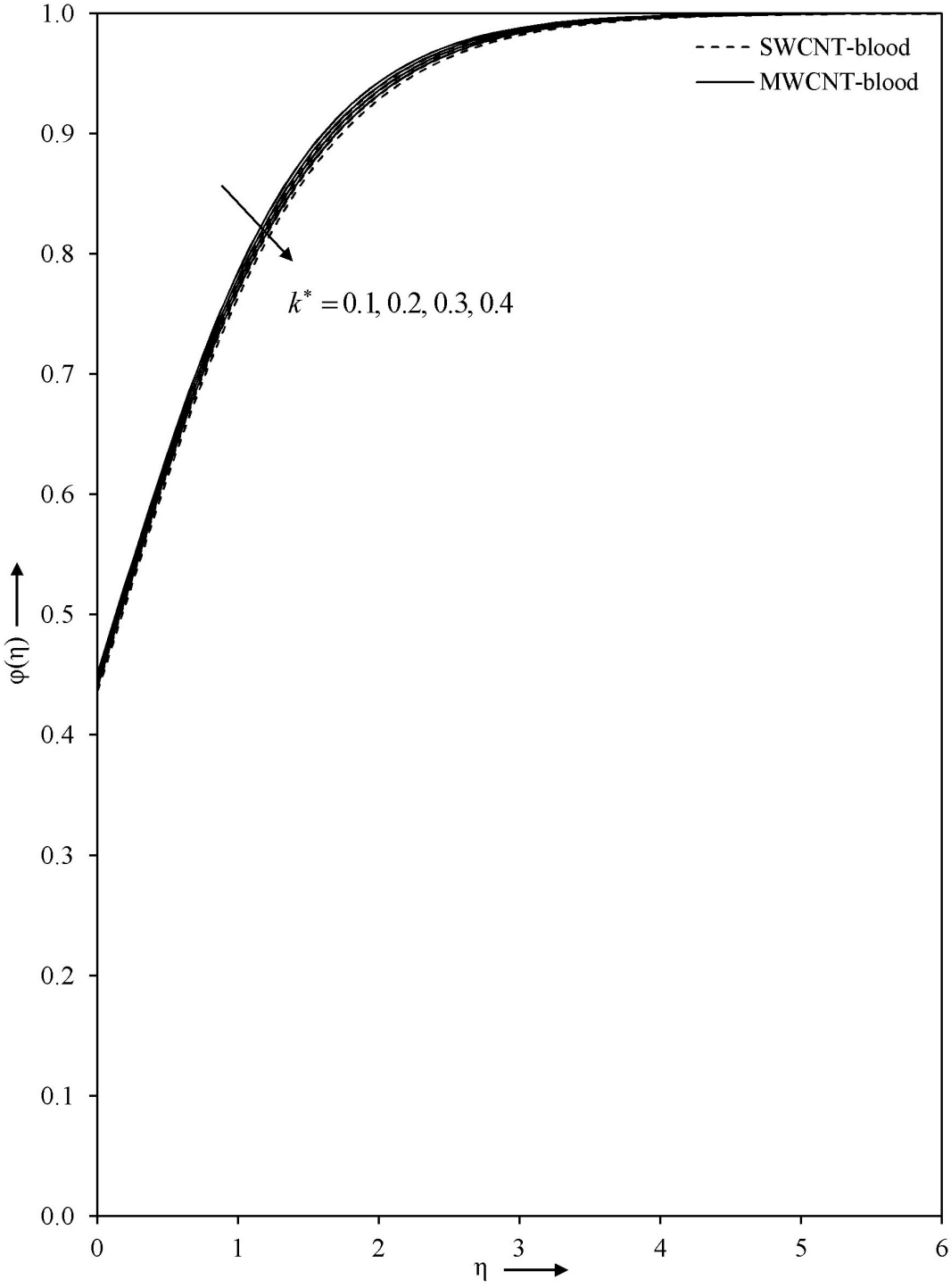

Figure 17: Impact of permeability parameter $k^\star$ on concentration profile with $m = 2.0$, $\alpha^\star = 0.1$, $A = 0.1$, $\phi = 0.1$, $Re_m = 0.1$, $K_s = 1.0$, $Sc = 1.5$ and $K = 0.5$

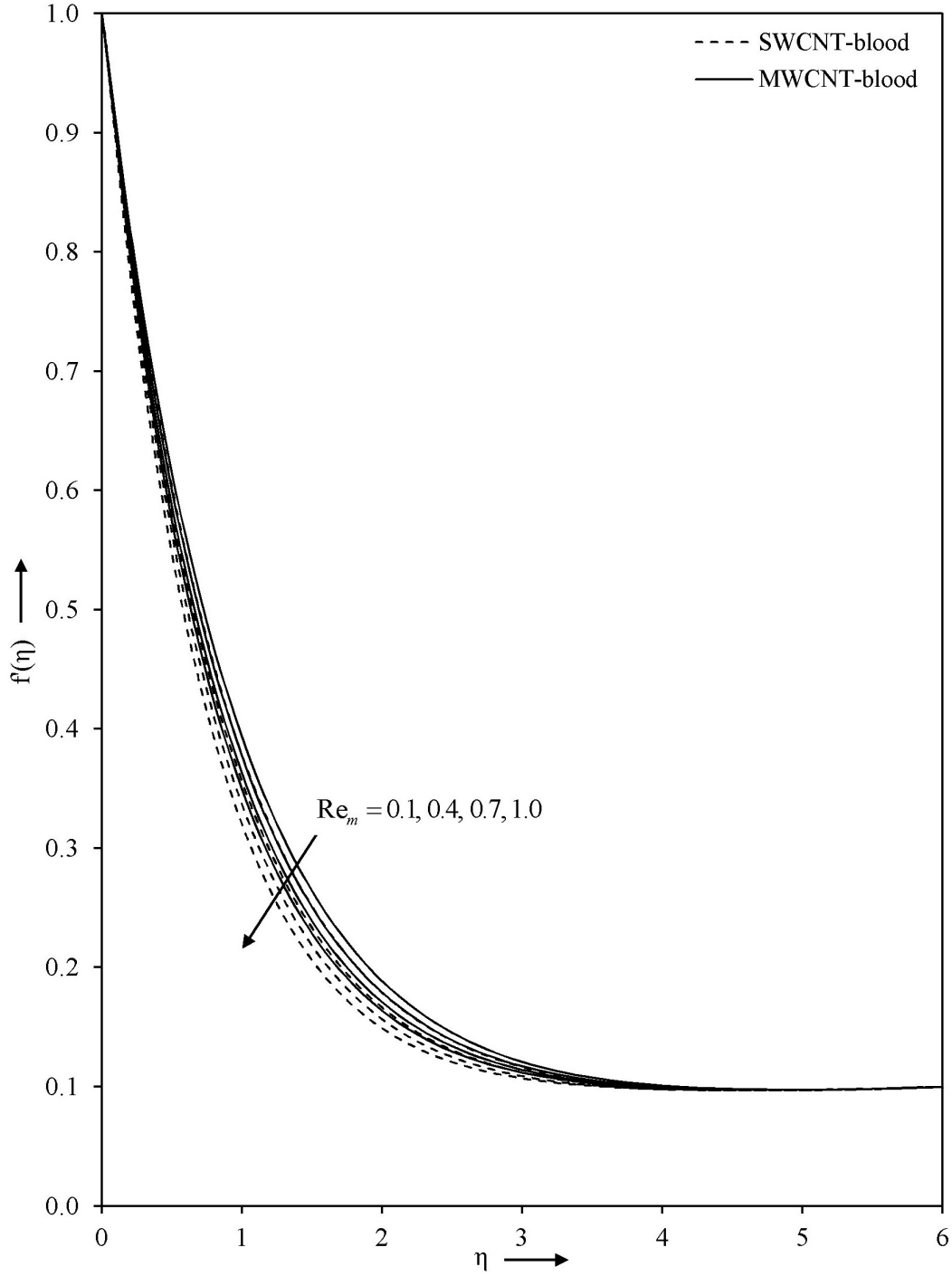

Figure 18: Impact of magnetic parameter Re_m on velocity profile with $m = 2.0$, $\alpha^\star = 0.1$, $A = 0.1$, $\phi = 0.1$ and $k^\star = 0.1$

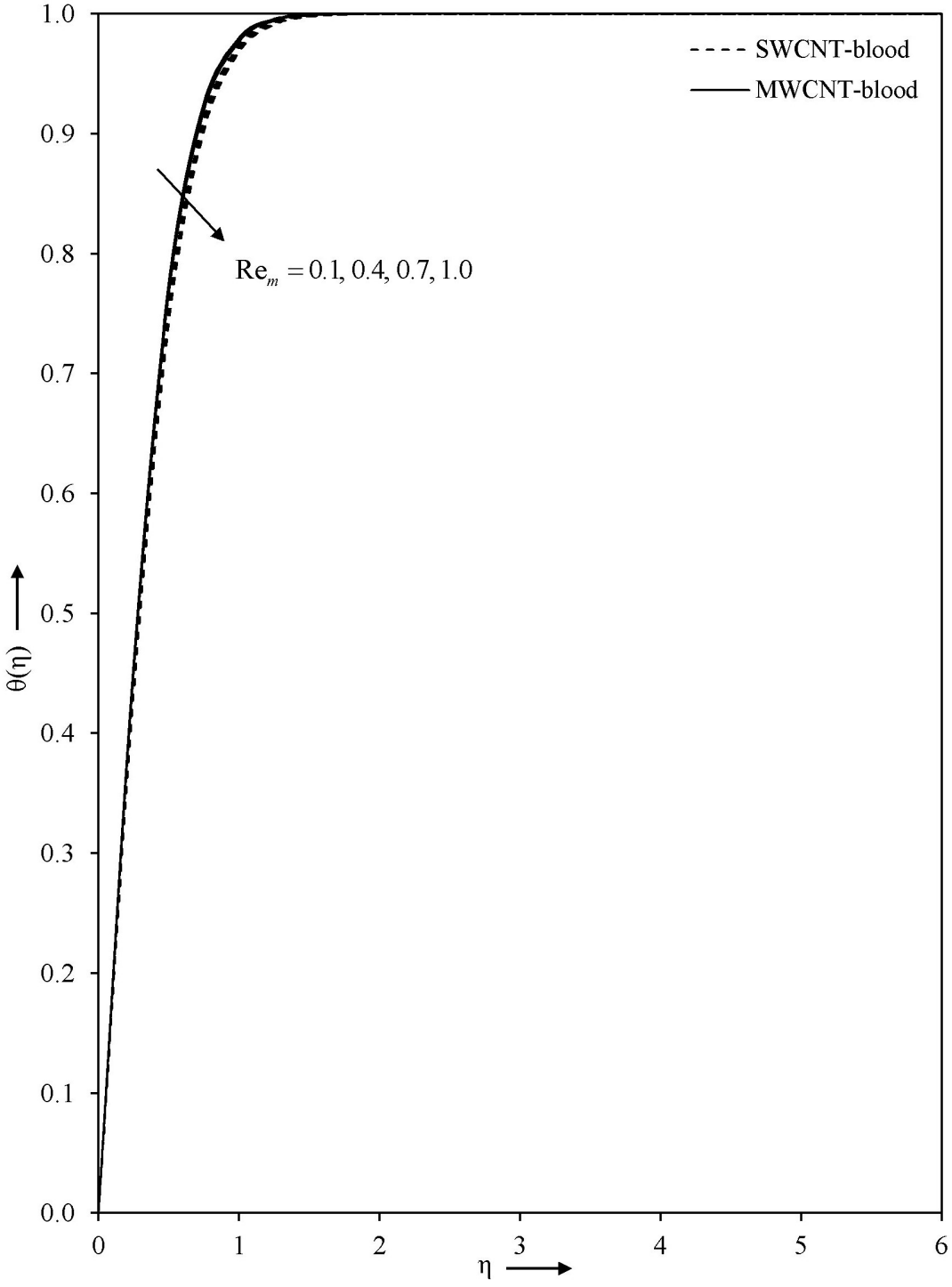

Figure 19: Impact of magnetic parameter Re_m on temperature profile with $m = 2.0$, $\alpha^\star = 0.1$, $A = 0.1$, $\phi = 0.1$, $k^\star = 0.1$, $Pr = 25$ and $Br = 0.1$

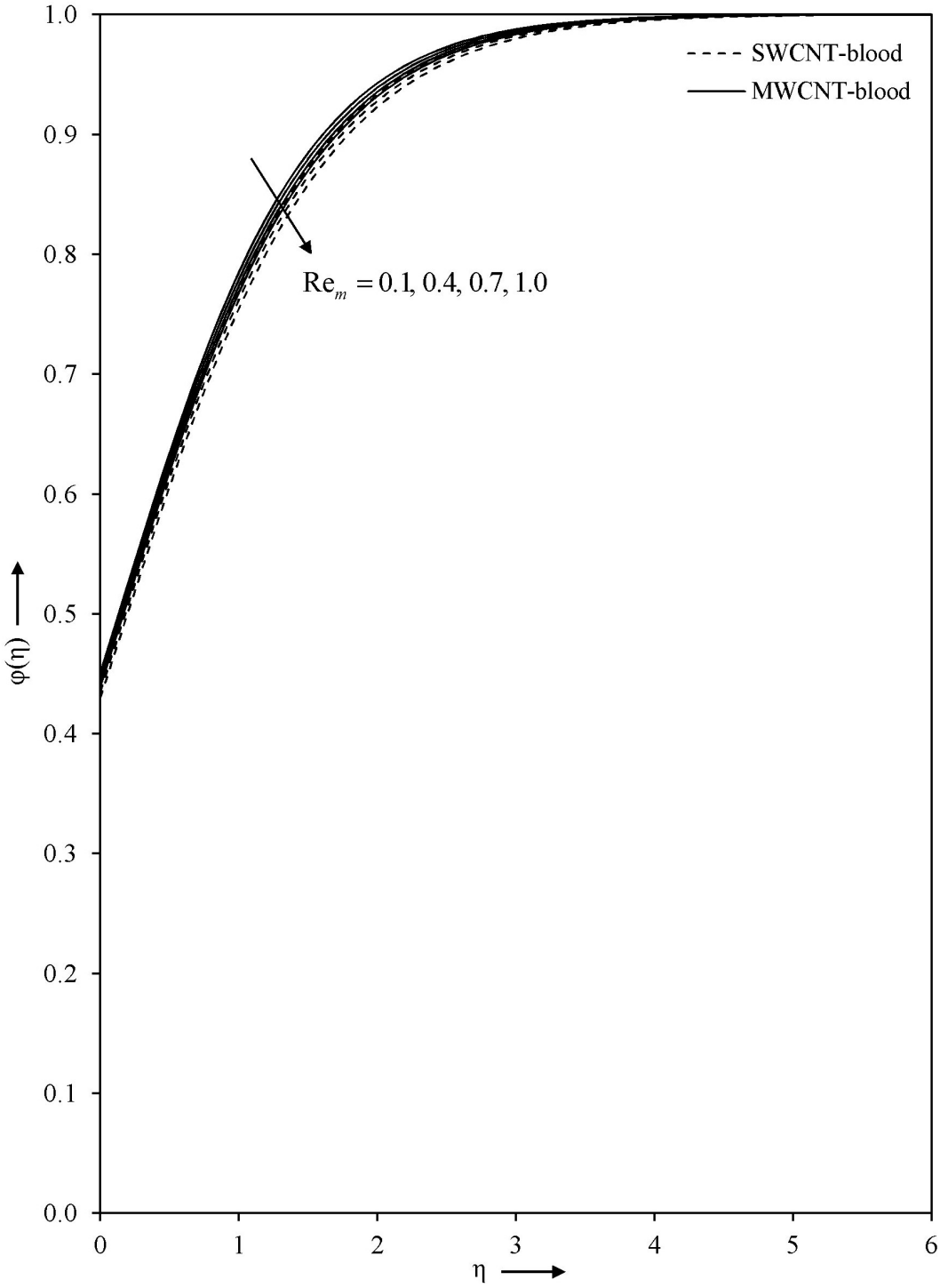

Figure 20: Impact of magnetic parameter Re_m on concentration profile with $m = 2.0$, $\alpha^\star = 0.1$, $A = 0.1$, $\phi = 0.1$, $k^\star = 0.1$, $K_s = 1.0$, $Sc = 1.5$ and $K = 0.5$

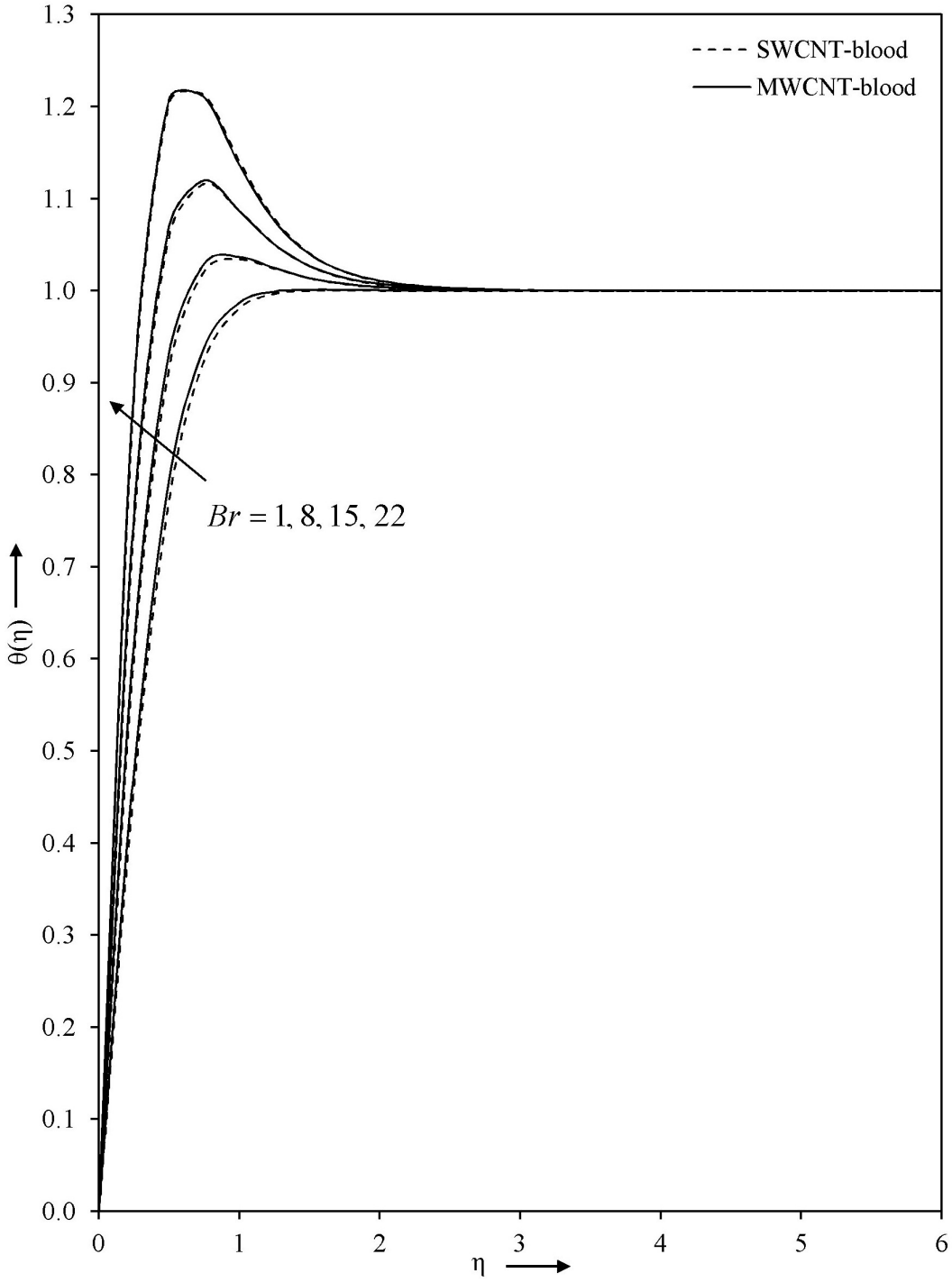

Figure 21: Impact of Brinkman number Br on temperature profile with $m = 2.0$, $\alpha^\star = 0.1$, $A = 0.1$, $\phi = 0.1$, $k^\star = 0.1$, $Re_m = 0.1$ and $Pr = 25$

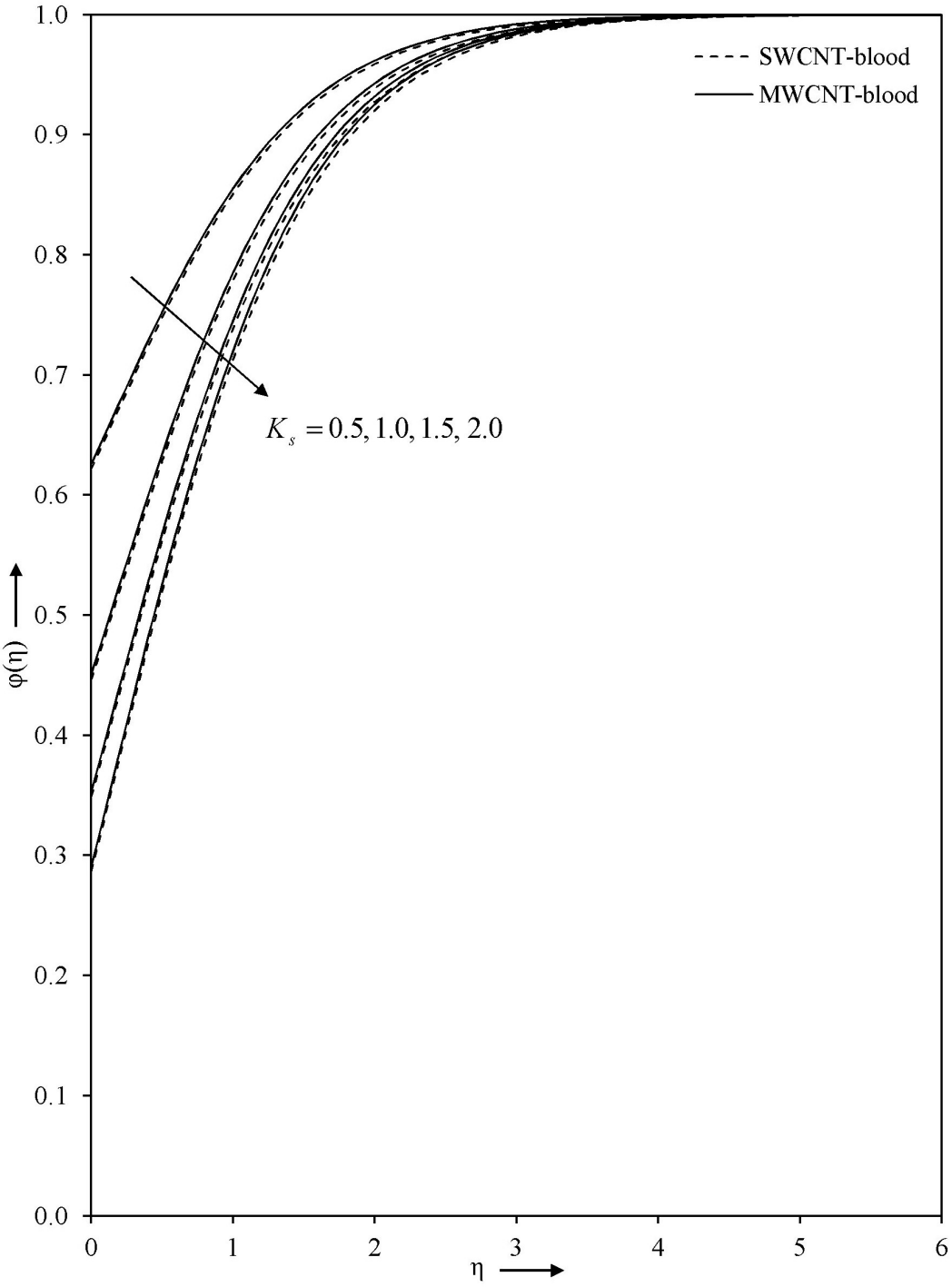

Figure 22: Impact of heterogeneous parameter K_s on concentration profile with $m = 2.0$, $\alpha^\star = 0.1$, $A = 0.1$, $\phi = 0.1$, $k^\star = 0.1$, $Re_m = 0.1$, $Sc = 1.5$ and $K = 0.5$

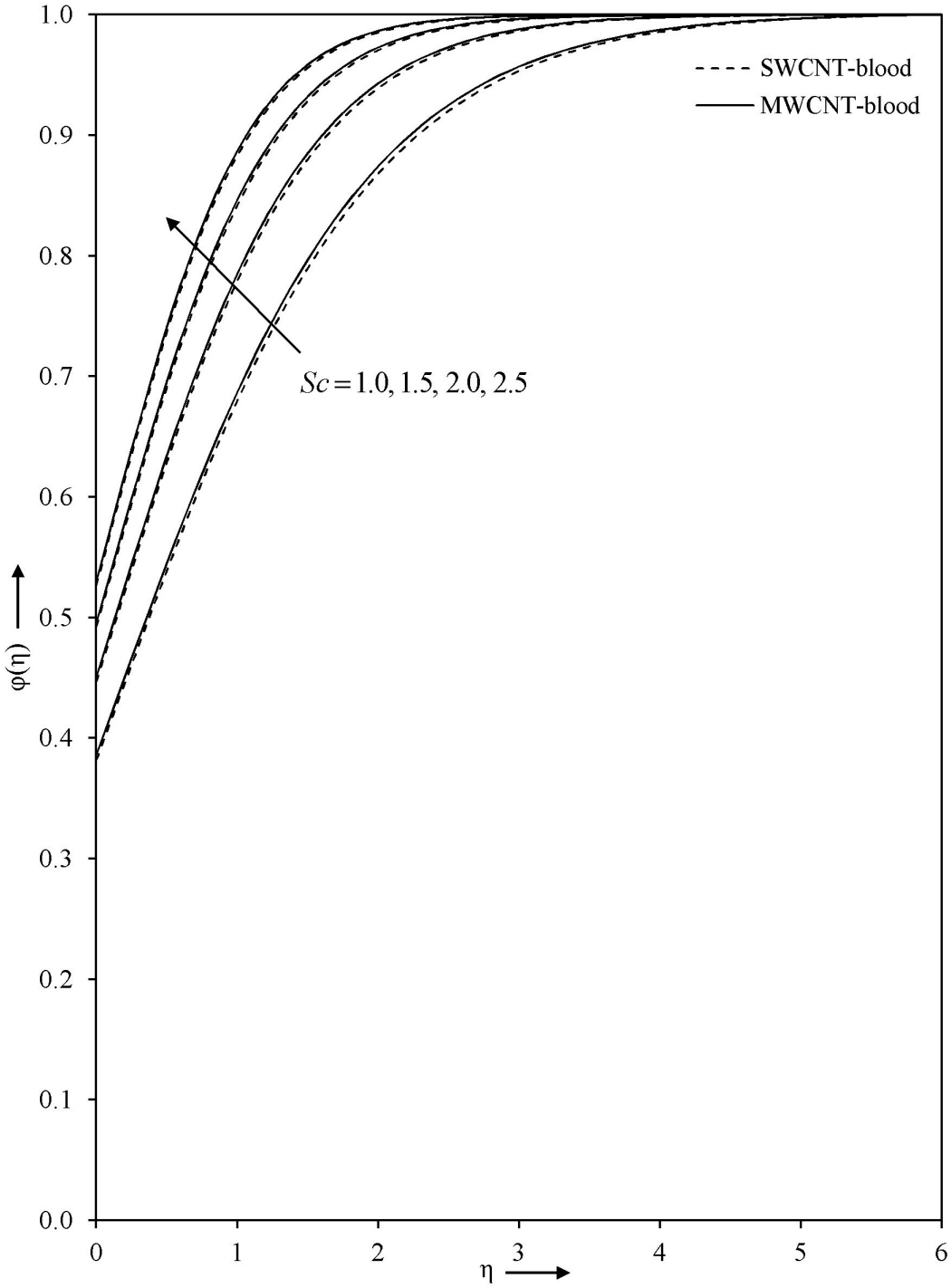

Figure 23: Impact of Schmidt number Sc on concentration profile with $m = 2.0$, $\alpha^{\star} = 0.1$, $A = 0.1$, $\phi = 0.1$, $k^{\star} = 0.1$, $Re_m = 0.1$, $K_s = 1.0$ and $K = 0.5$

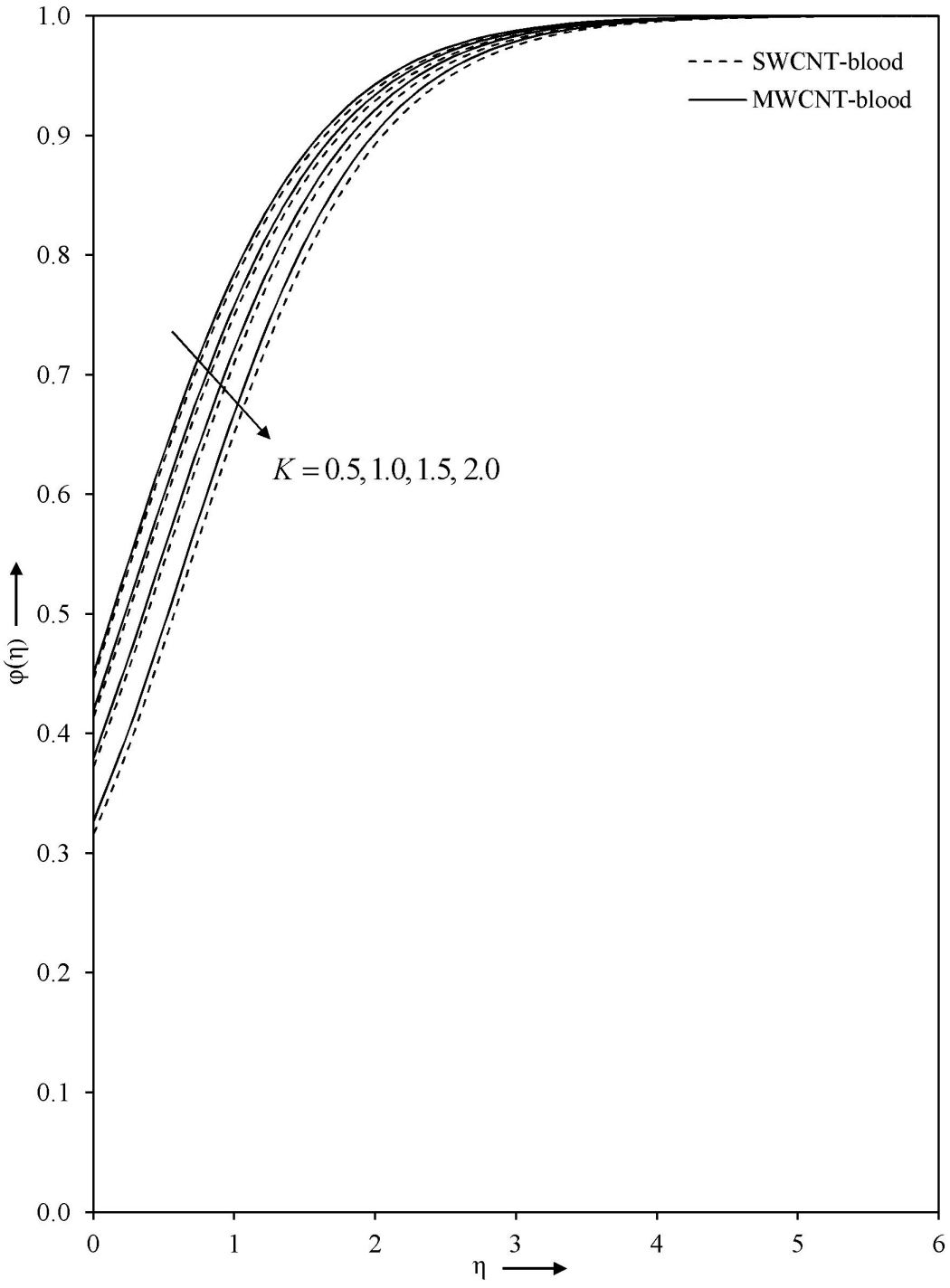

Figure 24: Impact of homogeneous parameter K on concentration profile with $m = 2.0$, $\alpha^{\star} = 0.1$, $A = 0.1$, $\phi = 0.1$, $k^{\star} = 0.1$, $Re_m = 0.1$, $K_s = 1.0$ and $Sc = 1.5$

Table III: Computed values of $f''(0)$, $\theta'(0)$ and $\varphi'(0)$ corresponding to various considered parameters for SWCNT−blood (SWCNT−b) and MWCNT−blood (MWCNT−b) with $Pr = 25$

m	$\alpha^\star$	A	ϕ	$k^\star$	Re_m	Br	K_s	Sc	K	$-f''(0)$		$\theta'(0)$		$\varphi'(0)$	
										SWCNT-b	MWCNT-b	SWCNT-b	MWCNT-b	SWCNT-b	MWCNT-b
0.1	0.1	0.1	0.10	0.1	0.1	0.1	1.0	1.5	0.5	0.885504	0.831434	2.4939	2.6089	0.44685	0.45354
1.0										1.007564	0.957639	2.0356	2.1204	0.39740	0.40156
2.0										1.053373	1.004705	1.8583	1.9318	0.36468	0.36780
3.0										1.075546	1.027434	1.7720	1.8400	0.34119	0.34375
2.0	0.4									1.014705	0.969169	1.3918	1.4357	0.33194	0.33556
	0.7									0.977555	0.934975	0.9902	1.0108	0.29657	0.30074
	1.0									0.941912	0.902115	0.6613	0.6658	0.25900	0.26372
	0.1	0.3								0.931354	0.890423	1.8888	1.9598	0.37987	0.38168
		0.5								0.742942	0.711969	1.9312	1.9997	0.39480	0.39580
		0.7								0.499347	0.480296	1.9810	2.0472	0.40845	0.40889
		0.1	0.01							1.108167	1.102490	3.0066	3.0276	0.36116	0.36152
			0.04							1.091644	1.070055	2.4754	2.5290	0.36220	0.36360
			0.07							1.073345	1.037454	2.1199	2.1870	0.36339	0.36569
			0.10	0.2						1.085488	1.038288	1.8515	1.9248	0.36200	0.36506
				0.3						1.116595	1.070738	1.8450	1.9180	0.35939	0.36237
				0.4						1.146767	1.102143	1.8386	1.9114	0.35680	0.35974
				0.1	0.4					1.128126	1.055586	1.8456	1.9232	0.35994	0.36457
					0.7					1.198385	1.104210	1.8336	1.9149	0.35550	0.36148
					1.0					1.264855	1.150847	1.8224	1.9070	0.35133	0.35853
					0.1	1.0				1.053373	1.004705	1.9820	2.0518	0.36468	0.36780
						8.0						2.9443	2.9850		
						15.0						3.9066	3.9183		
						22.0						4.8688	4.8515		
						0.1	0.5							0.25388	0.25532
							1.5							0.42743	0.43173
							2.0							0.46836	0.47350
							1.0	1.0						0.31166	0.31518
								2.0						0.40194	0.40468
								2.5						0.43004	0.43247
								1.5	1.0					0.33840	0.34258
									1.5					0.30425	0.31009
									2.0					0.25850	0.26700